Research Square

Preprints are preliminary reports that have not undergone peer review.
They should not be considered conclusive, used to inform clinical practice,
or referenced by the media as validated information.

Light-triggerable phage nanobots reduce neoplastic burden through precise photoablation of cancer cells

Paolo Emidio Costantini
University of Bologna
Sara Feola
University of Helsinki
Michela Nigro
University of Bologna
Luca Ulfo
University of Bologna
Roberto Saporetti
University of Bologna
Eleonora Turrini
University of Bologna
Alena Kaltenbrunner
University of Bologna
Maria Sofia Semprini
University of Bologna
Andrea Carboni
University of Bologna
Alessia Marconi
University of Bologna
Chiara Di Donato
University of Bologna
Manuela Sollazzo
University of Bologna
Monica De Luise
University of Bologna
Matilda Assirelli
University of Bologna
Pietro Cocco
University of Bologna
Annapaola Petrosino

University of Bologna
Manuele Di Sante
University of Bologna
Sara Cascone
University of Bologna
Carmela Fimognari
University of Bologna
Giuseppe Gasparre
University of Bologna
Anna Myriam Perrone
University of Bologna
Anna Maria Porcelli
University of Bologna
Pier Luigi Lollini
University of Bologna
Matteo Di Giosia
University of Bologna
Vincenzo Cerullo
University of Helsinki
Matteo Calvaresi
University of Bologna
Alberto Danielli
alberto.danielli@unibo.it

University of Bologna

Research Article

Keywords:

Posted Date: July 3rd, 2026

DOI: https://doi.org/10.21203/rs.3.rs-10131773/v1

License: This work is licensed under a Creative Commons Attribution 4.0 International License.
Read Full License

Additional Declarations: No competing interests reported.

Abstract

Engineered bacteriophages are gaining momentum in biomedical research, with outstanding potential in precision oncology. The opportunity to tweak phage tropism by displaying tumor-targeting moieties, together with the high molecular payload capacity, makes phage platforms particularly interesting for photo-oncolytic precision approaches, in which the cytotoxicity of otherwise harmless sensitizers is activated in situ by light irradiation. Here, we present the engineering of a light-triggerable M13 phage nanobot, displaying a single-domain antibody (sdAb) fused to the minor coat protein pIII, capable of delivering hundreds of Rose Bengal (RB) photosensitizer molecules to cancer cells expressing the epidermal growth factor receptor EGFR. We demonstrate that this vector is able to precisely seek out specific cell targets in a mixed cell population, and further validate its light-triggered cytotoxic efficacy in 2D and 3D tumor models. The phage bioconjugates significantly reduce tumor burden in epidermoid carcinoma murine xenografts upon a single intratumoral administration and irradiation with a focused light-emitting diode, and effectively photoablate human malignant ascites derived from patients with ovarian cancer. Collectively, our results provide compelling preclinical evidence for the photooncolytic efficacy of engineered phage-photosensitizer bioconjugates, paving the road for further translation of these modular and cost-effective platforms into the clinic.

Introduction

Bacteriophages (phages) are ubiquitous viruses that infect bacteria but are inoffensive to eukaryotic cells. Since their discovery, a century ago, they have had a huge impact on our understanding of the biological world, paving the road for fundamental discoveries and numerous translational applications [1]. Classic phage therapy, envisaging the use of natural lytic phages to control bacterial infections, has provided a useful tool before the advent of antibiotics [2,3]. More recently, both wild-type and engineered phage cocktails have been successfully applied in experimental antimicrobial precision therapies to treat patients near death from multidrug-resistant bacterial infections [4,5], without signs of adverse side effects. Likewise, simple non-lytic filamentous phages, such as M13 (or fd/f1), are receiving growing attention as well-defined protein-based platforms for the assembly of stable and biocompatible nanoscaffolds [6]. In principle, these phages can be retargeted to any type of cell through specific peptide or antibody display on the minor coat protein pIII, while therapeutic and imaging agents can be conjugated in hundreds of copies onto the phage capsid, providing a robust and flexible platform for anticancer approaches [7]. Clinically valuable oncotargeting single chain (scFv) and single domain antibodies (sdAb, VHH, nanobodies) are frequently selected by phage-display techniques [8,9], highlighting the robustness of M13 as tumor-targeting platform.

Oncotargeting M13 phages have recently been shown to be able to specifically vehiculate high payloads of light-triggerable photosensitizers (PSs), proving the effectiveness of phage-based nanovectors for targeted photodynamic therapy (PDT) [10–12]. PDT has been known since the early 1900s and represents a minimally invasive strategy for the ablation of a variety of solid tumors [13,14]. It is based on PS molecules

that can generate reactive oxygen species (ROS) upon excitation by light at a specific wavelength, provoking oxidative stress leading to cancer cell death [15]. Interestingly, PDT is also active on dormant and resistant cancer cells, as local ROS bursts generated during irradiation irreversibly impair membrane integrity and coarsely damage cellular macromolecules, including proteins and nucleic acids [14,16].

Yet, while phage-mediated photo-ablation has proven effective *in vitro* and in simple *in vivo* models including Hydra [17] and Zebrafish [18], a measure of its potency in mammals (mice) or patient-derived tumor specimens (*ex vivo*) is lacking, leaving the question open whether this approach could be applied to reduce neoplastic burden in operational (preclinical) settings.

To this sake, M13 phages were engineered to display a single-domain antibody (sdAb) targeting the Epidermal Growth Factor Receptor (EGFR), whose overexpression has been reported in a plethora of neoplasms, making it an ideal target for proof-of-concept validation of innovative therapies, including PDT [16,19]. After functionalization with Rose Bengal (RB), an FDA-approved ocular diagnostic stain and sensitizer for the treatment of various cancers [20,21], the engineered phage vectors were challenged to specifically seek out and ablate EGFR-expressing A431 epidermoid carcinoma cells and spheroids *in vitro*. The therapeutic efficacy of the phage-RB bioconjugates was then evaluated by testing whether they could reduce tumor burden in epidermoid carcinoma murine xenografts. We further tested their activity in EGFR-expressing patient-derived ascites from high-grade serous ovarian cancer, providing clinically relevant *ex vivo* validation of the platform.

The preclinical relevance of results and the emerging potential for further translation of this modular and scalable technology into the clinic are finally discussed.

Results

Pentavalent display of an EGFR-specific single domain antibody redirects M13 to selectively bind EGFR-positive cancer cells

To generate a robust EGFR-targeting phage nanovector, the 7D12 single domain antibody was leveraged [22]. A codon-optimized 7D12 sequence was cloned in frame with the C-terminal sequence of the g3p gene in a phagemid vector (GenBank: PX516380.1), allowing for pentavalent display of the 7D12-pIII fusion on the tip of the phage. $M13_{7D12}$ virions were generated using a Hyperphage helper, devoid of the *f1ori* packaging signal (Fig. 1A). Immunoblotting of the purified $M13_{7D12}$ virions with a pIII-specific antibody identified a band of about 40 kDa, corresponding to the expected molecular weight of the fusion protein (Fig. S1). Following the same engineering scheme, an aspecific control phage, $M13_{GHL}$, was generated (Fig. 1A), in which a peptide sequence (GHLIPLRQPSHQ), previously demonstrated to be aspecific for cancer cells [23], is displayed in fusion with pIII. The correct display of the targeting moieties was further validated in mass spectrometry [24], where the 7D12-pIII and GHL-PIII were identified at the expected molecular weights of 34.7 KDa and 22.8 KDa, respectively (Fig. 1B; S2-S3). The ability of these two nanovectors to target EGFR in a cellular system was evaluated on two different cell lines: A431,

derived from an EGFR-overexpressing human epidermoid squamous cell carcinoma, and RH4, derived from human alveolar rhabdomyosarcoma, lacking EGFR expression. Immunocytochemistry with an EGFR-specific monoclonal antibody (sc101, clone R1,) detected a strong signal on the surface of A431 cells (Fig. 1C), absent from the negative RH4 control (Fig. 1H), confirming the suitability of these lines for specificity testing of the retargeted phage nanovectors. To this end, both A431 and RH4 cell lines were incubated with either $M13_{7D12}$ or the $M13_{GHL}$ aspecific control, followed by incubation with an anti-pVIII FITC-labelled antibody to detect adsorbed phages. Upon incubation with $M13_{7D12}$ a strong fluorescence signal was observed on EGFR-positive A431 cells (Fig. 1D), while no signal was detected for the $M13_{GHL}$ control (Fig. 1E), or in controls without phage (Fig. 1F). Likewise, no signal was detected on the EGFR-negative RH4 line, even after incubation with $M13_{7D12}$ (Fig. 1I-1K), advocating specific binding mediated by 7D12 sdAb display.

These qualitative observations were further supported by quantitative flow cytometry analysis, which showed a distinct fluorescence peak shift encompassing nearly all of the A431 cell population, exclusively upon incubation with $M13_{7D12}$ (Fig. 1G) and absent in RH4 (Fig. 1L). Moreover, the mean fluorescence intensity (MFI) of A431 cells incubated with $M13_{7D12}$ was approximately two orders of magnitude higher with respect to $M13_{GHL}$ (Fig. 1M-N), while in RH4 no significant MFI difference between $M13_{7D12}$ and controls was detected (Fig. 1O-P). These results demonstrate that the specificity of $M13_{7D12}$ for EGFR-positive cells is entirely mediated by pIII display of the 7D12 sdAb at the tip of the phage.

Targeted payload delivery to EGFR-expressing cells by the M13 $_{7D12}$ vector.

The next objective was to assess the potential of $M13_{7D12}$ as nanovector for targeted molecular delivery. To this end, the CF594 fluorophore was conjugated onto the filamentous phage capsid, through the amines exposed by the highly regular and repetitive array of the pVIII major coat proteins (Fig. 2A). Following purification, the UV-Vis spectra of the phage bioconjugates (Fig. 2B; S4) showed the characteristic absorption band of CF594 dye confirming the successful functionalization of both $M13_{7D12}$ and $M13_{GHL}$. This was further substantiated by mass spectrometry analysis identifying the pVIII-CF594 product at 5948 Da, resulting from the covalent conjugation of CF594 (mw 729 Da) to the pVIII coat protein (mw 5237 Da) with the loss of a water molecule (Fig. 2C, S6). Taking advantage of CF594 fluorescent emission, phage-mediated molecular delivery of the fluorophore on both EGFR-positive (A431) and -negative (RH4) lines was evaluated. First, flow cytometric analysis was performed after incubation with the $M13_{7D12}$-CF594 bioconjugate or with a control $M13_{GHL}$-CF594 bioconjugate functionalized with a comparable number of fluorophores (Table S1). On the EGFR-positive A431 cell line, the fluorescence peak clearly shifted only after incubation with $M13_{7D12}$-CF594, with a ~ 430.0-fold increase in the mean fluorescence intensity (MFI) in comparison to the control (Fig. 2D, 2F). Conversely, in RH4 cells no shift or significant variation in MFI was observed for both $M13_{7D12}$-CF594 and $M13_{GHL}$-CF594 compared to PBS (Fig. 2E, 2G). These data demonstrate that the selected bioconjugation procedure does not alter the specific tropism of $M13_{7D12}$. Accordingly, we further challenged the

targeting ability of $M13_{7D12}$-CF594 in a competition assay, using a mixed A431 and RH4 cell population. To discriminate A431 and RH4 in flow cytometry, the latter were pre-incubated with Hoechst, a cell-permeant nuclear counterstain, allowing to detect EGFR-negative RH4 cells by blue fluorescence. A431 and RH4 cells were then mixed in a 1:1 ratio and $M13_{7D12}$-CF594 was added at a final concentration of 670 pM (corresponding to 300 nM of CF594). Increased fluorescence in the CF594 channel was only observed on EGFR-positive cells, while no significant change in RH4 fluorescence was detected (Fig. 2H-K). Remarkably, phage binding to A431 occurred rapidly within minutes, already plateauing after 15 minutes of incubation (Fig. 2K). To further validate specific binding in a mixed cell population, a confocal microscopy experiment was carried out. Both A431 and RH4 lines were labelled with calcein blue AM (Fig. 2L), while RH4 was also stained with calcein green AM (Fig. 2M). After incubation with $M13_{7D12}$-CF594, phage fluorescence was detected on the surface and inside A431 cells, with negligible signals visible on RH4 cells nearby (Fig. 2N-O). We conclude that $M13_{7D12}$ is able to seek out and selectively deliver light-responsive molecules to EGFR-positive cells, even in mixed population of cells, where aspecific uptake could potentially occur.

$M13_{7D12}$-RB bioconjugates mediate specific photoablation of EGFR positive cancer cells

We then evaluated the photooncolytic potential of EGFR-targeting phages after functionalization of the capsid with Rose Bengal (RB). RB is an FDA-approved anionic xanthene dye used in ophthalmology for over 30 years, characterized by excellent photosensitizing properties [20]. Chemical conjugation of $M13_{7D12}$ was performed *via* EDC/NHS cross coupling reaction between the amino groups of $M13_{7D12}$ capsid protein and the activated carboxylic-acid group of RB (Fig. 3A). Qualitative and quantitative assessment of phage conjugation was performed via UV-Vis absorption spectroscopy. The recorded spectra of the bioconjugate (Fig. S5) display both an absorption profile belonging to the M13 (λ_{max} 269 nm), and the absorption profile of the RB (λ_{max} 570 nm). As further confirmation of successful conjugation to the pVIII protein, mass spectrometry analysis confirmed the presence of the pVIII-RB conjugate at the corresponding mw of 6193 Da (Fig. 3B; S6). The ability of the $M13_{7D12}$-RB bioconjugates to generate ROS upon irradiation was assessed in a phantom system, using Amplex Red and ABMDMA assays, which enabled the quantification of hydrogen peroxide and singlet oxygen, respectively (Fig. S7). Results indicated that $M13_{7D12}$-RB are characterized by a high photoactivity and generate ROS following both type I and type II mechanism. Upon conjugation to the phage, RB produces more hydrogen peroxide and less singlet oxygen compared to the free PS. This shift from energy transfer process (type II mechanism) to electron transfer process (type I mechanism) after conjugation to proteins has already been described for RB [12], as well as for other PSs [25]. This finding is particularly significant, as the development of new type I photosensitizers is an area of rapidly growing interest. In contrast to type II PSs, type I PSs retain their activity under hypoxic tumor conditions, are less dependent on molecular oxygen, and produce a broader range of ROS, thereby promoting more extensive and effective anticancer activity. The ability to generate ROS was retained also in a more complex cellular environment. A431

cells were irradiated for 60 seconds with a portable, focusable and single wavelength light emitting diode (565 nm, light dose 0.07 J/cm²) after incubation at different phage concentrations, while negative controls were kept in the dark. Upon irradiation, a phage concentration-dependent increase in intracellular ROS was observed, whereas ROS levels remained comparable to baseline in non-irradiated controls (Fig. 3C). We conclude that irradiated $M13_{7D12}$-RB bioconjugates are able to generate a burst of ROS, which may drive the specific photoablation of targeted cells. This hypothesis was further investigated on both A431 and RH4 cell lines. After incubation with increasing concentrations of $M13_{7D12}$-RB or free RB equivalents, cells were washed to remove any unbound or aspecifically adsorbed phage virions or sensitizer molecules. The cells were then irradiated for 60 seconds with the same LED used for the ROS assay, while controls were kept in dark. No dark cytotoxicity was observed, even at the highest phage concentration (Fig. 3D), indicating high cytotolerance of the vectors in the absence of the triggering light. Conversely, a specific and dose-dependent decrease in viability was observed upon irradiation of the cells incubated with the phage. At 1 μM of RB equivalents delivered by $M13_{7D12}$, the viability of EGFR-positive A431 cells decreased to 19.7 ± 5.1 %, whle the EGFR-negative RH4 cell line exhibited minimal cytotoxicity (85.4 ± 6.7 % of iable cells; Fig. 3E). This result emphasizes the specificity of photoablation mediated by the retargeted $M13_{7D12}$-RB phage.

Furthermore, no cytotoxic effect was detectable for free RB, at any of the concentrations tested, proving that the bioconjugated $M13_{7D12}$ phage enhances the photooncolytic activity of RB by selectively delivering the sensitizer to EGFR-positive cells (Fig. S8, S9). Notably, this cytotoxic effect was achieved at sub-nanomolar concentrations of the engineered phage, reflecting the high payload capacity of M13 for targeted photodynamic applications. Comparable light-triggered cytotoxic effects were observed under both short, localized LED irradiation and prolonged broadband illumination conditions (Fig. S8), highlighting the robustness of the system across different irradiation modalities.

Beyond cellular uptake, another major limitation of PDT is its dependence on molecular oxygen, which is required for the generation of cytotoxic ROS and is often poorly available in hypoxic solid tumors [26,27]. To directly assess whether reduced oxygen availability affects $M13_{7D12}$-RB-mediated photoablation, the experiment was repeated on A431 cells under controlled hypoxic conditions at 1% O_2. The results closely mirrored those obtained under normoxic conditions, indicating that the light-triggered cytotoxic efficacy of the system is retained even when oxygen availability is strongly reduced (Fig. 3F).

Specific oxidative stressors can activate a range of molecular cell death pathways, including but not limited to necrosis, apoptosis and autophagy [13]. To distinguish between regulated and non-regulated forms of cell death (e.g apoptosis or necrosis) induced in $M13_{7D12}$-RB photoablated cells, the Guava Nexin Assay (Luminex) was used. By focusing on membrane integrity, this assay represents a robust marker that allow discerning between cells in the early stages of regulated cell death (Annexin-V+/7-AAD-) and necrotic ones with compromised cell membranes (Annexin-V+/7-AAD + or Annexin-V-/7-AAD+). Upon irradiation, most A431 dying cells exhibited a necrotic profile, whereas < 1% of the events aligned to a programmed apoptotic cell death at both the RB concentrations tested (0.1 and 0.3 μM)

(Fig. 3G). In accordance with cell viability data (Fig. 3D), dark controls did not show any Annexin-V and/or 7-AAD positive staining (Fig. 3H). These results indicate that under the fluence conditions tested, $M13_{7D12}$-RB vectors promote necrotic cell death, likely deriving from permanent damage to membrane structures, as previously observed also with a thiophene-derivative sensitizer [17].

M13-RB nanobots disrupt tumor spheroids upon light activation

Immortalized cell lines serve as foundational models; however, three-dimensional in vitro models are gaining prominence due to their capacity to better emulate the biochemical and biomechanical interactions inherent to the actual cytoarchitectures in tumor microenvironment [28]. Accordingly, we cultured and matured EGFR-expressing A431 homospheroids, to evaluate the performance of $M13_{7D12}$-RB-mediated photoablation in a simple 3D model. A431 spheroids were incubated with 3 μM sensitizer equivalents (Fig. 4), either in the free form (RB), or conjugated to the phage vector ($M13_{7D12}$-RB). Spheroids not incubated with sensitizers were also included as negative controls. Following irradiation (3 min; light dose: 0.21 J/cm²), or incubation in the dark, spheroids were visualized by confocal microscopy and assessed for viability using a 3D-optimized bioluminescence kit (Promega).

Spheroids kept in dark conditions preserved their structural integrity (Fig. 4A-C; S10A-C), displaying no significant decrease in cell viability (Fig. 4G). After irradiation, the untreated spheroids maintained their three-dimensional configuration (Fig. 4D; S10D) and those incubated with free RB displayed minor changes, evidenced by the presence of a few floating cells, detached from the spheroids (Fig. 4E, S10E). On the contrary, spheroids incubated with $M13_{7D12}$-RB exhibited a pronounced disruption of 3D cytoarchitecture upon irradiation (Fig. 4F; S10F), accompanied by a marked reduction in cell viability (Fig. 4H). These observations establish a direct association between the compromised spheroid structure and the photoablation mediated by $M13_{7D12}$-RB.

Phage-mediated photoablation reduces tumor burden in murine xenografts

To further evaluate the ability of $M13_{7D12}$-RB to penetrate and deliver the payload in a more complex and relevant system such as a solid tumor, an *in vivo* model of A431 was reproduced in nude mice.

To define the most effective phage administration route *in vivo*, we first conducted a biodistribution experiment to evaluate the tumor targeting of unconjugated $M13_{7D12}$ vectors upon both intratumoral (IT) and intravenous (IV) injection (Fig. 5A-B). Quantitative PCR analysis revealed detectable phage accumulation in tumor tissue following both administration routes. In the case of IV administration, phage levels were higher in tumors compared to other analysed organs, although this difference did not reach statistical significance (Fig. 5A). In contrast, IT administration resulted in a significantly higher accumulation of phages in tumor tissue compared to all other organs tested (Fig. 5B).

Based on this marked and statistically significant tumor enrichment, the IT route was selected for subsequent *in vivo* efficacy studies. Accordingly, the photo-oncolytic potential of $M13_{7D12}$-RB bioconjugates was evaluated in an A431 xenograft model in nude mice. Considering on the absence of detectable dark toxicity in the preceding *in vitro* assays, the *in vivo* efficacy study compared mock-treated mice, injected with PBS and not irradiated, with mice receiving a single IT injection of $M13_{7D12}$-RB (15 μM RB equivalents) followed by light irradiation. Irradiation was performed for 5 minutes at day 6, immediately after phage administration, and repeated at day 8 without additional phage injection using the same focused LED source described above (light dose: 0.45 J/cm²; Fig. 5C). Tumor growth was monitored for each group through the study and was significantly slower in $M13_{7D12}$-RB treated mice compared with the mock controls (Fig. 5D). These results indicate that phage-RB bioconjugates can significantly reduce neoplastic burden in an epidermoid carcinoma xenograft model, supporting their potential for light-triggered anti-tumor treatment.

M13-RB supports effective photoablation of High-Grade Serous Ovarian Carcinoma-derived ascites

Recalling the ability of engineered phages to penetrate three-dimensional tumor spheroids [11,17,18] and even tumor heterospheroids (A. Kaltenbrunner & J. Prakash; personal communication), we set out to validate the oncolytic potential of $M13_{7D12}$-RB on two ascites derived from patients affected by High-Grade Serous Ovarian Carcinoma (HGSOC). Owing to their heterogeneous composition in terms of cancer cells, immune cells such as T-lymphocytes and macrophages, as well as non-cancer epithelial and mesenchymal cells [29], ascites have a key role in the proliferation, progression, immune evasion and chemoresistance of ovarian cancer [30]. In HGSOC patients, ascitic fluid represents a reservoir of aggressive neoplastic cells that actively contribute to disease dissemination. Given these features, patient-derived ascites constitute a valuable *ex vivo* model to assess the efficacy of targeted therapeutic approaches in a complex and physiologically relevant tumor microenvironment. In particular, the cancer cell fraction can persist as single entities or more often as multicellular aggregates, the latter constituting an unequivocal and most malignant component of HGSOC ascitic fluid [31,32]. Starting from a collection of samples derived from HGSOC patients, we selected two ascites specimens whose genetic screening, as previously described [33], showed a cellular fraction almost entirely composed by neoplastic cell aggregates. Such method exploits the knowledge that more than 96% of HGSOC harbour pathogenic mutations in the tumor suppressor *TP53*, and their retrieval is indicative of cancer abundance in specimens such as ascitic fluids, as we have shown [33]. Indeed, Sanger sequencing of the ascites-derived cellular fraction confirmed the presence of the same primary tumor-associated *TP53* pathogenic alterations, i.e. the homozygous nonsense c.637C > T (p.R213*) at a known *TP53* hotspot in specimen 1, and the heterozygous frameshift deletion c.450del (p.T150fs) in specimen 2 (Fig. S11), indicating a high representation of neoplastic cells in both specimens. EGFR expression levels in ascites were investigated by immunofluorescence microscopy using anti-EGFR commercial antibody (SC-101, clone R1). Prominent fluorescent signals for EGFR were observed in both specimens (Fig. 6A-F), validating

expression of the receptor targeted by the engineered phage. The ability of $M13_{7D12}$ to perform payload delivery in *ex vivo* samples was hence assessed by incubating patient-derived ascites with $M13_{7D12}$-CF594, which resulted in a fluorescence pattern distribution of distinct spots similar to those observed with anti-EGFR mAb (Fig. 6G-L). The phage ability to photoablate EGFR-expressing ascites was investigated by incubation with $M13_{7D12}$-RB (3 μM RB equivalents) followed by irradiation (3 min; light dose 0.21 J/cm²), revealing a marked decrease in ascites cell viability (58.8 ± 7.6 % and 50.8 ± 8.0 % rspectively) (Fig. 6M, 6O). In contrast, no significant reduction was detected in samples kept in the dark (Fig. 6N, 6P) or pre-incubated with free RB. This latter observation is particularly compelling, indicating that ascite ablation is strongly boosted by the targeted sensitizer delivery prompted through phage vector binding. Consistently, confocal microscopy analysis showed a pronounced disruption of the ascitic cytoarchitecture upon treatment with $M13_{7D12}$-RB combined with light irradiation, whereas untreated samples maintained a compact multicellular organization (Fig. S12). Together the results demonstrate remarkable potential of $M13_{7D12}$-RB phage bioconjugates to mediate effective tumor photoablation also on complex, malignant and clinically relevant, patient samples, paving the road to precision oncology applications.

Discussion

Targeting moieties and nanovectors rigged with photo-activatable sensitizers represent a promising approach for immunomodulatory precision oncology approaches [34,35]. This potent double-targeting therapy combines the accumulation of photosensitizers at malignant cells with the possibility to irradiate a focused area, ensuring a powerful spatiotemporal control of cytotoxicity towards cancer cells, reducing off-targets and the collateral damage to healthy tissues [36]. EGFR constitutes an attractive oncotarget for PDT, due to its overexpression and amplification in several tumors with severe outcomes and poor prognosis [37–40], well exemplified by the recent FDA approval of Cetuximab-IRDye700DX (ASP-1929) bioconjugates for the treatment of EGFR-positive cancers [41]. In fact, conditional excitation of the EGFR-targeted sensitizers by light allows to trigger cytotoxicity only at the tumor site, sparing other EGFR-expressing cells. Bacteriophages represent less explored delivery agents for targeted photodynamic ablation, but are strongly emerging as a convenient oncotargeting platform, allowing to combine powerful genetic phage display technology with photochemical functionalization strategies of the virion capsid [3,7,42,43]. Compared to purely synthetic scaffolds, phage therapeutics have shown excellent pharmacodynamics, biocompatibility and body clearance [4,5].

Herein, we have engineered a M13 phage-based nanovector highly specific for EGFR, capable of precisely delivering hundreds of light-triggerable sensitizers to target EGFR-expressing cancer cells, demonstrating for the first time effective phage-mediated photoablation potential in preclinically relevant *in vivo* and *ex vivo* mammalian cancer models. EGFR targeting of the phage vector was achieved by phage display of the 7D12 single-domain antibody, validated for targeted PDT in previous preclinical studies [44–47]. 7D12 recognizes an epitope located on human EGFR domain 3 and comprises residues

that are essential for the recognition of EGF, such as arginine 355 (D355), allowing it to mimic the inhibitory properties of the intact monoclonal antibody drug Cetuximab [48]. Pentavalent expression of 7D12 on $M13_{7D12}$ resulted in the acquired tropism of the phage towards EGFR-positive cells, leading to the formation of a phage corona surrounding EGFR-expressing cancer cells and also to phage internalisation into the cytoplasmic compartment, likely because of receptor-mediated endocytosis of the receptor [49–51]. This feature allowed precise and specific molecular delivery to EGFR-expressing cells, also in complex multicellular environments, including mixed cell populations, A431 homospheroids and malignant ascites. These results fully align with recent observations indicating that phages, particularly M13, are able to penetrate and cross very efficiently biological barriers [50,52,53], including the tumor microenvironment (TME)[18,54]. This feature is particularly relevant for solid tumor therapy, where tissue penetration is a key determinant of therapeutic efficacy and large biologics or antibody-drug conjugates (ADCs) often suffer from poor penetration into the TME [55,56]. In this context, different tumor-targeting phage platforms developed in recent years have shown activity in complex models, including 3D tumor spheroids [11,17], zebrafish xenografts [18], and murine tumors [51,57]. Consistently, in our system, free equimolar RB failed to impair spheroid cytoarchitecture or significantly affect cell viability, whereas $M13_{7D12}$-RB induced marked spheroid disruption upon irradiation, highlighting the ability of M13 nanovectors to enhance photodynamic performance by increasing targeted sensitizer delivery to tumor cells. Nevertheless, current knowledge on the photodynamic efficiency of phage-sensitizer bioconjugates in more complex, preclinically relevant, tumor models is still a matter of debate. Biodistribution analysis after IT and IV administration of $M13_{7D12}$ nanobots in epidermoid carcinoma mouse xenografts showed significant tumor retention after IT injection, supporting this route for the subsequent efficacy study. After IV administration, phage levels were detectable in tumor tissue and approximately one order of magnitude higher than in the other analysed organs, although this enrichment did not reach statistical significance. These data suggest that systemic delivery may enable tumor access, but further studies will be required to define the robustness and therapeutic relevance of this route. Accordingly, the in vivo efficacy demonstrated here should be interpreted in the context of IT administration, while the therapeutic potential of systemic delivery remains to be established and will require careful evaluation of phage clearance through the liver and spleen by the mononuclear phagocytic system [50]. However, while liver accumulation and hepatotoxicity are well-recognized concerns for many nanoparticles [58] and biotherapeutics, including ADCs [59,60], off-target accumulation of M13-sensitizer conjugates is not expected to generate substantial toxicity in the absence of irradiation, as the phage vectors are harmless without light activation. In addition, the dose of RB equivalents administered through the phages to mice (< 0.2 mg/kg mouse body weight), is not expected to generate hepatotoxicity in the absence of photoactivation, as it falls within the 0.01–10 mg/kg range previously reported as well tolerated in rodents, with biliary excretion without further processing [61–64]. Moreover, RB has long been used to assess liver function, biliary tract patency and hepatobiliary conditions [62–64]. In parallel, the coevolution of microbiota phages with the human host rendered the M13 virion well tolerated, biomimetic [65], and only moderately immunogenic. This represents an advantage in photo-oncolytic applications, as it can contribute to boost anti-tumor immune-responses [66], especially upon

PDT-induced immunogenic cell death (ICD) [67,68]. Indeed, PDT can trigger different forms of ICD and promote the release of damage-associated molecular patterns (DAMPs), thereby stimulating both innate and adaptive immune responses [67,68]. Importantly, unlike systemic immunotherapy that can trigger autoimmune effects, immunomodulatory responses triggered by photo-induced ICD and ROS cytotoxicity [67] remain spatially confined to the irradiated area, reducing the risk of systemic toxicity [69,70]. Consistently, our $M13_{7D12}$ nanobots showed low pro-inflammatory activity in this cellular setting, as indicated by the absence of detectable IL-6 and TNFα release in A431 cells after phage exposure (Fig. S13), and were harmless to cells in the dark, independently of EGFR expression.

Upon irradiation, cells targeted by the $M13_{7D12}$-RB nanobots underwent non-programmed cell death, a feature previously observed in PDT, which may depend on several factors such as the cell type, the sensitizer chemistry, its cellular location, the duration and fluence rate of light exposure, and the oxygen availability [16,68,71]. When exposed to light, photosensitizers that localize to the mitochondria typically promote apoptosis, whereas those that localize to the plasma membrane typically induce membrane blebbing [17,72,73], followed by rapid loss of cell integrity, causing substantial physical damage to the cell [74], and consequent impairment of regulated cell-death mechanisms. Following phage administration and irradiation, the number of cells with damaged membranes increased significantly, correlating with RB concentration. Similar results were also obtained with RB conjugated to M13 phage retargeted to colon cancer cells [11], while Ce6 conjugated to retargeted M13, co-localised with mitochondria, and was shown to induce autophagic cell death [10]. Beyond subcellular localization and cell death modality, oxygen availability represents another key determinant of PDT efficacy. We observed that the rates of photoablation mediated by $M13_{7D12}$-RB under hypoxic conditions were comparable to those obtained under normoxia, suggesting a reduced dependence of the system on oxygen availability. Such resilience may derive, at least in part, from the high local photosensitizer payload delivered by the phage nanovector, which can sustain effective ROS generation under low-oxygen conditions. In addition, the shift toward a type I PDT mechanism of RB conjugates, may partially alleviate the dependence of the system on molecular oxygen availability [75,76]. Since hypoxic tumor regions are characterized by reduced but not completely depleted oxygen levels [26,77], these findings support the potential applicability of $M13_{7D12}$-RB in poorly oxygenated tumor areas. Collectively, these findings suggest that the high payload delivery enabled by the phage nanovector, combined with its retained efficacy under hypoxic conditions, contributes to mitigating two major limitations of conventional PDT, namely inefficient sensitizer delivery and oxygen dependence. Noteworthy, the efficacy of $M13_{7D12}$-RB bioconjugates in sensitizer delivery and cancer photoablation was also confirmed in human *ex vivo* samples derived from ascites of HGSOC patients. HGSOC-derived ascites represent a valuable preclinical model as they recapitulate many features of the tumor microenvironment, including malignant aggregates and non-malignant stromal/immune components [29]. Accordingly, human ascites have been used to evaluate anticancer therapies and oncolytic viruses [30]. The ascites presented in this study were characterized as mainly composed of malignant cells and shown to overexpress EGFR, which generally correlates with greater invasiveness, aggressiveness and metastasis in ovarian cancer [78]. The uptake of nanoparticles and

subsequent drug delivery is highly variable between patients due to the heterogeneous nature of malignant cells, both within a patient and throughout a patient population [35]. In addition, multicellular structures derived from ascitic fluid are enriched in extracellular matrix and collagen, which can shield cells from nanoparticle targeting [79]. In this respect, the effective targeting and photoablation of ascitic cells mediated by the $M13_{7D12}$-RB nanobots upon irradiation represent a first and consistent validation of the translational potential of engineered photo-oncolytic M13 vectors, further strengthened by the efficacy in reducing epidermoid carcinoma neoplastic burden in a murine xenograft model.

The key advantage of targeted M13 phage nanobots for photoablation not only relies on their high payload delivery and ability to penetrate biological barriers, but also on the modularity of the phage display platform and their scalable biomanufacturing. Indeed, phage display enables the genetic fusion of diverse targeting moieties, as exemplified by the recurrent selection of clinically relevant tumor-targeting ligands (peptides, scFv, sdAb, VHH, nanobodies, DARPins, Pronectins, Affibodies, monobodies, etc.) in pharmaceutical discovery pipelines. Furthermore, biomanufacturing scalability also represents a valid asset of this platform over other biotherapeutics and phage scaffolds, due to the non-lytic nature of M13, allowing continuous production under GMP in large industrial fermentors, with 10-fold lower estimated production costs per dose (~ 1$ for 10^[12] pfu) as compared to therapeutic mAbs [80]. Besides, M13 has a 10-to 100-fold higher cargo payload on the capsid over ADCs, resulting in higher potency (e.g. active at subnanomolar vector concentrations [12,17]). The pentavalent display of tumor-targeting moieties on the pIII minor coat protein may further enhance target engagement through avidity effects. Finally, the existence of hundreds of filamentous phages belonging to the *Inoviridae* family grants a virtually unlimited source of alternative virion scaffolds onto which the phage vector technology could eventually be grafted [81,82], with the advantage of eluding the formation of anti-vector antibodies in case of repetitive treatments.

In conclusion, the results reported in this work represent a fundamental step in advancing the development of phage-based nanovectors for precision oncology approaches, providing strong preclinical evidence for the efficacy of engineered M13 nanobots as tumor-seeking, photo-oncolytic and cost-effective platform for targeted PDT, with interesting translational potential and excellent biomanufacturing scalability.

Methods

Phage engineering and production

The nucleotide sequence encoding the 7D12 anti-EGFR nanobody (see SI for complete nucleotide and amino acidic sequence) was obtained as a synthetic gene and amplified by PCR using primers AD0276 (GTTTTGAGCTCCAGGTTAAATTAGAGGAGTC) and AD0277 (GTTTTACTAGTGCTAGATACCGTCACTTGAGTA), introducing SacI and SpeI restriction sites. The amplified fragment was digested and directionally cloned into the SacI/SpeI-linearized pComb3XSS phagemid (Addgene), generating the pComb3XSS_7D12 construct. Similarly, the nucleotide sequence

encoding the control GHL peptide was cloned following the same strategy. In this case, oligonucleotides AD323 (CGGCCATCTGATTCCGCTGCGCCAGCCGAGCCATCAGCAGA) and AD324 (CTAGTCTGCTGATGGCTCGGCTGGCGCAGCGGAATCAGATGGCCGAGCT) were annealed to generate a double-stranded insert with compatible SacI and SpeI overhangs, which was then ligated into the SacI/SpeI-linearized pComb3XSS vector. The recombinant phagemids were co-transformed into *E. coli* DH5α with the helper phage plasmid derivative lacking the f1 origin (M13KO7Δg3pΔoriF1), allowing the production of recombinant virions packaging exclusively the phagemid and displaying the nanobody-pIII fusion, as previously described [83]. Co-transformed cells were grown in LB medium supplemented with ampicillin (100 mg L^{-1}), kanamycin (25 mg L^{-1}), and 0.4 mM IPTG for 24 h at 37 °C. Phage virions were purified from the culture supernatant by PEG/NaCl and isoelectric point precipitation. Briefly, cultures were centrifuged at 12000 g for 20 min, and the supernatant was supplemented with PEG 8000 (4% w/v) and NaCl (3% w/v), followed by incubation on ice for 1 h. Phages were pelleted by centrifugation (12000 g, 20 min) and resuspended in PBS 1×. Further purification was performed by isoelectric precipitation at pH 4.2, corresponding to the M13 isoelectric point, followed by centrifugation at 12000 g for 10 min. The purified phage ($M13_{7D12}$) was finally resuspended in PBS 1×. Phage concentration was determined by measuring the absorbance at 269 nm using a UV–Vis spectrophotometer and applying an extinction coefficient of ε = 3.84 cm^2 mg^{-1}.

Phage bioconjugation and characterization

Phage bioconjugation

Chemical functionalization of M13 phage vectors was performed by exploiting the reactivity of surface-exposed amine groups on the pVIII coat proteins. For Rose Bengal (RB) conjugation, the photosensitizer was first chemically activated to generate a reactive ester intermediate, which was subsequently incubated with purified phage suspensions under buffered conditions, enabling covalent coupling to capsid proteins. CF594 labeling was achieved by direct reaction of the dye with phage capsid amine groups in mildly basic buffer conditions, allowing efficient conjugation without affecting the targeting moiety displayed on pIII. Following the conjugation reactions, phage–dye bioconjugates were purified to remove unreacted dye and reaction by-products. Purification was performed by dialysis against PBS in sterile conditions. The degree of functionalization and dye-to-phage ratios obtained across independent preparations are reported in Table S1.

Phage characterization

The UV-vis spectroscopic characterization of phage bioconjugates, was performed with a Cary60 UV-Vis spectrophotometer (Agilent). Phage quantification was achieved by monitoring the absorption band centered at 269 nm according to Smith's formula [84]. Quantification of the dyes was performed at absorption max 594 nm for CF594 (ε= 115,000 $M^{-1}cm^{-1}$) and 571 nm for RB (ε= 90,000 $M^{-1}cm^{-1}$).

High-performance liquid chromatography (HPLC) coupled to electrospray ionization Time-of-Flight mass spectrometry (ESI-ToF MS) was performed to characterize denatured intact capsid proteins as recently

described by Kaltenbrunner et al. [24]. Briefly, the proteins were precipitated according to Wessel et al. [85], and the pellet was washed with methanol, dried, and stored at -20 °C. The pellet was resuspended in formic acid [86] and chromatographic separation was achieved with an ACQUITY UPLC 2.1x150 mm Protein BEH C4 column (300 Å pore size, 1.7 µm particle size) operating at 0.4 ml/min flow and 65 ˚C on an ACQUITY UPLC H-Class PLUS system (Waters). The separation employed eluent A (HPLC-grade water, 0.1% formic acid) and B (acetonitrile, 0.1% formic acid) as following: 0-1 min step at 10% B, 1-18 min gradient at 50% B, 18-20 min step at 50% B, 20-21 min gradient at 90% B, 21-23 min step at 90% B, 23-24 min gradient down to 10% B, 24-26 min step at 10% B. The setting for MS detection on a Xevo G2-XS quadrupole Time-of-Flight (QToF) mass spectrometer was: capillary voltage 2.5 kV; sample cone 60 V; source temperature 150 ˚C; desolvation temperature 600 ˚C; cone gas 50 L/h and desolvation gas 900 L/h. Data analysis and mass spectra deconvolution were achieved using Unidec software 5.0.2 version (University of Oxford, Oxford, UK) [87].

Cell cultures and in vitro models

2D cell culture

The A431 human epidermal carcinoma cell line was propagated in RPMI 1640 medium supplemented with 10% heat inactivated fetal bovine serum (FBS), 1% penicillin–streptomycin solution 100 U ml^{-1} and 1% l-glutamine 200 mM (Euroclone, Italy). The RH4 human rhabdomyosarcoma cell line was cultivated in DMEM medium supplemented with 10% heat inactivated FBS, 1% penicillin–streptomycin solution 100 U ml^{-1} and 1% l-glutamine 200 mM (Euroclone, Italy). Cells were grown at 37 °C in a humidified incubator with 5% CO_2. For hypoxia experiments, A431 cells were cultured in a hypoxia workstation (INVIVO 200, Ruskinn Technology Ltd, Bridgend, UK) under controlled low-oxygen conditions (1% O_2).

Spheroid generation

Spheroids of A431 cells were cultured utilizing low adhesion multi-well plate, 96U Bottom Plate from Nunclon Sphera (Thermo Fisher Scientific, Waltham, MA, USA). A total of 500 cells were dispensed into each well in a volume of 100 µL. Following seeding, the plates were incubated at 37 °C in a 5% CO_2 environment for 5 days, allowing the cells to aggregate and form spheroids. To maintain optimal culture conditions, 50% of the medium was refreshed every third day. Precision in liquid handling was ensured using an automated multichannel pipette, operating at a dispensing rate of 10 µL/s, sourced from Gilson, Middleton, WI, USA. Over a 5-day observation period, the spheroids exhibited steady, exponential, and uniform growth. Upon successful formation of the microtissues, the spheroids were carefully transferred upon a cover slip and secured into the AttoFluor™ Cell Chamber (Thermo Fisher Scientific). This allowed for detailed microscopic analyses.

Targeting and imaging assays

Flow cytometry

For quantitative assessment of EGFR expression, 1 × 10^6 cells were collected in 2ml tubes, centrifuged at 900 g for 5 min and resuspended in 1 mL complete medium. Cells were fixed using 4% paraformaldehyde (PFA) for 15 min at room temperature (RT), washed with wash buffer (PBS supplemented with 0.05% Tween-20), and blocked in 2% (w/v) milk in wash buffer for 45 min at RT. Cells were incubated with anti-EGFR antibody (1:500, antibody R1 (Santa Cruz Biotechnology)) for 1 h, washed twice with wash buffer, and subsequently incubated with Alexa Fluor® 488-conjugated goat anti-mouse IgG (1:1000, Invitrogen) for 1 h at RT. After two final wash buffer washes, cells were resuspended in 300 µL of PBS.

Similarly, for quantitative evaluation of tropism, 1 × 10^6 cells were incubated with 10^12 $M13_{7D12}$ phages in complete medium for 45 min at 37 °C. After washing twice with wash buffer, cells were fixed with 4% PFA for 15 min and blocked with 2% milk for 45 min. Samples were stained with anti-pVIII antibody (1:500, ProGen) for 1 h, followed by Alexa Fluor® 488-secondary antibody (1:1000) for 1 h.

Tropism of conjugated phages was performed on live cells as follows: cells (3 × 10^5 per well) were seeded in 6-well plates and incubated overnight at 37 °C. After 24h, cells were exposed to phages, $M13_{7D12}$-CF594 (1 µM final concentration) in 500 µL of complete medium for 45 min at 37 °C. After incubation, cells were washed twice with PBS, detached with 1× trypsin for 5 min at 37 °C, and resuspended in complete medium. Following centrifugation at 900 g for 5 min, pellets were resuspended in 300 µL PBS for analysis. NT controls (no phage incubation) were included. Flow cytometric analyses were performed on a Beckman Coulter CytoFLEX S flow cytometer. Cell populations were gated on forward and side scatter parameters. Alexa Fluor 488 emission was detected in the FITC channel (excitation 488 nm, emission 525/40 nm). Additional fluorophores were recorded as follows: RB in PE (561 nm → 585/42 nm), CF594 in ECD (561 nm → 610/620 nm). Median fluorescence fold-increase over controls was used to quantify receptor expression or phage binding.

Regarding the competition assay, A431 and RH4 were mixed and stained with Hoechst 33342 and $M13_{7D12}$-CF594 (0,3 µM) and analyzed after 1, 5 and 10 minutes. At least 10,000 events per sample were recorded. Data were analyzed using CytExpert (Beckman Coulter) and FlowJo (BD Biosciences).

Confocal microscopy

To evaluate the EGFR expression on the A431 and RH4 cell lines, 3 × 10^4 cells were seeded onto round glass coverslips (12 mm, VWR) placed in 6-well plates (Corning, USA) in complete medium and incubated overnight at 37 °C under 5% CO_2. The following day, coverslips were gently washed and fixed with 4% paraformaldehyde (PFA) for 15 min at room temperature. Cells were then washed twice with PBS containing 0.05% Tween-20 (wash buffer), permeabilized using 0.1% Triton X-100 in PBS for 10 min and subsequently blocked in 2% skim milk (w/v) in wash buffer for 45 min at RT under gentle shaking. Cells were incubated for 1 h with anti-EGFR monoclonal antibody (1:500, antibody R-1 (Santa Cruz Biotechnology)) diluted in 2% skim milk (w/v) in wash buffer, washed twice with wash buffer, and stained for 1 h with Alexa Fluor® 488-conjugated goat anti-mouse secondary antibody (1:1000, Invitrogen).

Nuclei were counterstained with Hoechst 33342 (1 µg mL^{-1}, 15 min), and coverslips were mounted in PBS.

To visualize the receptor-specific phage binding, 3 × 10^4 cells were seeded on a glass coverslip and incubated overnight at 37 °C. Cells were treated with 500 µL complete medium containing 1 × 10^12 $M13_{7D12}$ phages. After 45 min incubation at 37 °C, cells were washed twice with PBS, fixed with 4% PFA for 15 min, permeabilized with 0.1% Triton X-100 for 10 min, and blocked with 2% milk in wash buffer for 45 min. Phages were detected using anti-pVIII monoclonal antibody (ProGen, 1:500) for 1 h, followed by Alexa Fluor® 488-conjugated secondary antibody (1:1000) for 1 h. Nuclei were stained with Hoechst 33342 for 15 min, and coverslips were mounted in PBS.

For studying the tropism of bioconjugated $M13_{7D12}$, cells were seeded, incubated with phages and washed as already described. Next, live cells were stained for 15 min with Hoechst 33342, and the fluorescence of CF-594 or RB was monitored.

Regarding the competition assay, cells were stained with calcein blue and only the RH4 with calcein green, after two washes with PBS the cells were seeded and treated for 45 minutes with $M13_{7D12}$-CF594 (0,3 µM final concentration). Imaging was performed on a Nikon A1R confocal microscope under identical acquisition settings for all conditions.

Irradiation setup and in vitro light-triggered assays

Irradiation setup

Light-triggered experiments were performed using a mounted LED source (M565L3, Thorlabs; nominal wavelength = 565 nm, FWHM 104 nm, output power 880 mW, viewing angle 125°) operated in contact mode with the sample to ensure localized and reproducible illumination. The LED was driven by a T-Cube LED driver (1200 mA) and coupled to an aspheric condenser lens system to achieve focused irradiation. For in vitro (2D and 3D) and ex vivo experiments, the LED source was positioned in direct contact with the culture plate. For *in vivo* experiments, the LED was applied in direct contact with the tumor site. Irradiation parameters are reported as light doses (J/cm^2), calculated from the nominal irradiance and exposure time. As an alternative irradiation setup, a broadband white LED lamp (Valex 30 W) was used at a fixed distance of 20 cm from the cell plate, corresponding to an irradiance of approximately 24 mW/cm^2 at the sample plane. Irradiation was performed for 30 minutes and was exclusively applied for cell-free ROS generation assays (Amplex Red and ABMDMA) as well as for preliminary cytotoxicity screenings in 2D cultures reported in the Supplementary Information.

Analysis of ROS generation

Intracellular ROS production was assessed using the ROS-Glo™ H_2O_2 assay (Promega). Briefly, 20,000 A431 cells were seeded in 96-well plates and incubated with increasing concentrations of $M13_{7D12}$-RB (up to 1 µM of RB) for 45 minutes. After incubation, cells were washed twice with PBS to remove excess

phage and irradiated for 1 minute in PBS using a 565 nm LED source. Following irradiation, ROS-Glo reagent was added to each well and cells were incubated for 20 minutes at room temperature. Luminescence was measured using an EnSpire® multimode plate reader (PerkinElmer).

To further investigate ROS generation in a cell-free system, complementary assays were performed to quantify hydrogen peroxide and singlet oxygen production. Hydrogen peroxide generation was evaluated using the Amplex Red assay. Samples containing free RB or $M13_{7D12}$-RB were prepared in 50 mM phosphate buffer (pH 7.4) and irradiated under defined conditions before reagent addition. Following irradiation, Amplex Red working solution containing horseradish peroxidase (HRP) was added, enabling the conversion of the non-fluorescent probe into the fluorescent product resorufin in the presence of peroxides. Fluorescence emission was measured, and hydrogen peroxide concentrations were determined by interpolation on calibration curves generated using hydrogen peroxide standards. Singlet oxygen production was evaluated using 9,10-anthracenediyl-bis(methylene) dimalonic acid (ABMDMA) as a chemical probe. The disodium salt of ABMDMA reacts with singlet oxygen to form an endoperoxide, resulting in a progressive decrease in absorbance that can be monitored spectrophotometrically. Iso-absorbing solutions of free RB and $M13_{7D12}$-RB were prepared in deuterated PBS (10 mM, pH 7.4). Reaction mixtures (500 µL) containing 15 µM RB equivalents and 25 µM ABMDMA were maintained under constant stirring and irradiated with a visible light source (white LED, irradiance ≈ 24 mW cm^{-2} at the sample surface). The decrease in ABMDMA absorbance at 401 nm was recorded over time and used to quantify singlet oxygen generation. The singlet oxygen quantum yield (ΦΔ) of $M13_{7D12}$-RB was estimated by using free RB as a reference (ΦΔ = 0.76 in deuterated PBS). Relative values were calculated from the slopes of ABMDMA photobleaching curves according to the relationship $\Phi\Delta,S = (kS/kR) \times \Phi\Delta,R$, where k represents the rate of absorbance decay for the sample (S) and reference (R), respectively.

In vitro cell viability assay

Cell viability in 2D cultures was assessed using MTT assays. Briefly, culture medium was removed and replaced with fresh medium supplemented with MTT at a final concentration of 0.5 mg mL^{-1}, and cells were incubated at 37 °C with 5% CO_2 for 90 minutes. The MTT-containing medium was then removed and replaced with DMSO to solubilize the formazan crystals. Absorbance was measured at 570 and 690 nm using an EnSpire® multimode plate reader (PerkinElmer, USA). Cell viability was evaluated 24 hours after treatment.

Cell viability in 3D models was evaluated using the CellTiter-Glo® 3D assay (Promega), which measures ATP levels as an indicator of metabolically active cells. Following treatment and irradiation, spheroids were incubated for 24 hours under standard culture conditions. Subsequently, spheroids were transferred to an opaque 96-well plate and incubated with CellTiter-Glo® 3D reagent according to the manufacturer's instructions. Plates were shaken to ensure complete lysis and luminescence was recorded using an EnSpire® multimode plate reader (PerkinElmer). The luminescence signal, proportional to ATP content, was used to determine relative cell viability.

Analysis of cell death mechanisms

To investigate the cellular death pathways induced by $M13_{7D12}$ bioconjugated phages, A431 cells (2×10^5 per well) were seeded in 24-well plates and incubated overnight (~16 h). Cells were then treated with increasing concentrations of M137D12-RB (0, 0.1 and 0.3 μM RB equivalents) for 45 minutes at 37 °C. Following incubation, cells were washed twice with PBS to remove unbound phages and subsequently irradiated for 1 minute using a 565 nm LED source or kept in the dark as controls. After irradiation, cells were resuspended in complete RPMI medium and further incubated under standard conditions. 6 hours post-treatment cells were washed, detached using 1× trypsin for 3–5 minutes, and resuspended in PBS prior to staining. For analysis, 100 μL of cell suspension were mixed with 100 μL of Guava Nexin reagent (Luminex), containing annexin V-phycoerythrin (PE) and 7-aminoactinomycin D (7-AAD). Samples were incubated for 20 minutes at room temperature in the dark and subsequently analysed by flow cytometry using a CytoFLEX S flow cytometer (Beckman Coulter).

Cytokine release assay

To assess whether phage exposure induced a pro-inflammatory response in this cellular setting, cytokine release was evaluated in A431 cells following incubation with unconjugated ($M13_{7D12}$) or RB-conjugated ($M13_{7D12}$-RB) phages in the absence of light activation. Cells were treated with phages (~10^11 particles), PBS (negative control), or doxorubicin (1 μM, positive control) for 3 hours, followed by washing and further incubation under standard culture conditions. Cytokine production was quantified using luminescence-based immunoassays (Lumit® IL-6 (Human) and Lumit® TNFα (Human), Promega), measuring interleukin-6 (IL-6) at 24 hours and tumor necrosis factor alpha (TNFα) at 6 hours post-treatment. Detailed experimental conditions and data analysis are reported in the Supplementary Information.

Animal experiments

In vivo biodistribution

All *in vivo* biodistribution experiments were performed in accordance with Italian and European regulations and approved by the Italian Ministry of Health (authorization 282/2024-PR). Solid tumors were established by subcutaneous injection of 1×10^6 A431 cells into the right flank of six-week-old female Hsd Nude Foxn1nu mice (Envigo). Treatments were initiated when tumors reached 350-400 mm^3, as measured by calipers. Tumor volumes were calculated as $V=(\pi/6) \times (\sqrt{ab})^3$, where a is the maximal tumor diameter and b is the maximal diameter perpendicular to a. Tumor-bearing mice were divided into three groups: untreated controls (n = 3), intravenous (IV) administration (n = 4), and intratumoral (IT) administration (n = 4). Mice in the IV group received 100 μL of $M13_{7D12}$ (10^12 phages) via tail vein injection, whereas mice in the IT group were injected directly into the tumor with 10 μL (10^11 phages).

After 24 hours, mice were euthanized and tissues including tumor, liver, spleen, and stomach, were collected, flash-frozen in liquid nitrogen, and stored at −80 °C until analysis. For DNA extraction,

approximately 25 mg of tissue were homogenized and processed using the ReliaPrep™ gDNA Tissue Miniprep System (Promega) for the initial lysis step, including incubation with proteinase K and cell lysis buffer overnight at 56 °C. Following lysis, a phenol-chloroform extraction was performed. DNA was quantified by spectrophotometry and used for downstream analysis.

Phage's DNA levels were quantified by real-time PCR using primers AD211 (tccggccttgctaatggtaa) and AD 212 (cgcaaagacaccacggaata), specific for a conserved phage sequence. Reactions were performed using PowerUp SYBR Green Master Mix (Applied Biosystems) in a final volume of 10 µL, with 0.4 µM primers and 2 µL of template DNA, and run on a CFX Connect Real-Time PCR Detection System (BioRad). Absolute quantification was obtained using a standard curve generated from serial dilutions of phage DNA. All samples were analyzed in technical triplicates.

In vivo phage-mediated tumor photoablation

All animal experiments were reviewed and approved by the Experimental Animal Committee of the University of Helsinki and the Provincial Government of Southern Finland (license number ESAVI/6678/2019). Six-week-old female HsdCpb: NMRI-Foxn1nu nude mice were obtained from Envigo (Laboratory, Bar Harbor, Maine). The human epidermoid carcinoma model EGFR+ (A431) was subcutaneously injected (1×10^6 cells) into the right flank of each mouse. Treatment was initiated at day 6 post tumor implantation, when tumors were palpable and measurable by caliper, with mean volumes of approximately 50–60 mm^3 across groups. In line with the 3R principles and based on the absence of detectable dark toxicity observed in the preceding *in vitro* assays, the efficacy study was performed using two experimental groups. Mice in the treatment group (n=5) received a single intratumoral injection of $M13_{7D12}$-RB (15 µM RB equivalents, corresponding to approximately 3 × 10^13 phage virions), followed by 5 minutes of irradiation using a 565 nm LED source. A second irradiation was performed at day 8 post tumor implantation without additional phage administration. Mock-treated mice (n=5) were injected with PBS and were not irradiated. Tumor volumes were measured with a caliper every two days and calculated using the formula $V = (L \times W^2)/2$, where L is the longest tumor diameter and W is the shortest perpendicular diameter. Mice were euthanized once humane endpoints were reached.

HGSOC-derived ascites: collection, characterization and treatment

Ascites collection

Two different ascitic fluid samples derived from a HGSOC patient collection enrolled in the MiPEO study (107_2011_U_Tess), approved by the local ethical committee at S. Orsola Hospital, Bologna, were selected on the basis of their physiologically prominent cancer cells enrichment. The samples were processed as reported in [33]. Briefly, for each patient, collected ascitic fluids were centrifuged at 500 g for 15 min at room temperature (RT). The precipitate was resuspended in a solution of ammonium chloride-based Red Blood Lysis Solution 1X (Miltenyi Biotec, #130-094-183) and incubated for 15 min at RT to rupture erythrocytes. Ultimately, a centrifugation step at 300 g for 5 min at RT was performed. The

haemolyzed cell pellet was washed in PBS, a part aliquoted in tubes, centrifuged at 15,000 g for 2 min and stored at −80°C for genetic analyses. The remaining cell pellet was used for cryopreservation and preparation of subsequent immunofluorescent analyses.

DNA extraction and TP53 sequencing

DNA from ascitic cell pellets was isolated by using QIAamp DNA Blood mini kit (QIAGEN, #51106) following manufacturer's instructions. Briefly, ascitic cell pellets were resuspended in 200 µL of PBS and 20 µL of proteinase K. Then, 200 µL of lysis buffer AL were added, samples were mixed by pulse-vortexing for 15 s (sec), and incubated for 10 min at 56°C. Next, 100% ethanol was added. Samples were then transferred into QIAamp Mini spin columns, centrifuged at 6,000 g for 1 min and the flow-through was discarded. Two washes were performed using Buffer AW1 and AW2. Finally, samples were eluted by centrifugation at 6,000 g for 1 min after 5 min incubation in 100 µL of nuclease-free water. DNA quantification was performed at NanoDropTM 2000 Spectrophotometer (Thermo Scientific). 20 ng of DNA was amplified by PCR and sequenced using *TP53* primers targeting exon 6 for ascites sample 1 and exon 5 for ascites sample 2, as previously described [33]. Representative electropherograms were visualized using Chromas software (Technelysium Pty Ltd, South Brisbane, Australia). Variants were compared to the TP53 reference transcript NM_000546.5 (NCBI RefSeq).

EGFR immunofluorescence in ascites samples

Thawed ascitic fluid derived cells were resuspended in 10 mL of DMEM F12 culture medium and put in culture for 2 days to allow physiological recovery before the analyses. After this time, ascites samples were incubated with Hoechst (#33342 Thermo Fisher Scientific) for 40 min a 37°C for nuclei staining, then collected in tubes and centrifuged at 300 g for 5 min. The supernatant was discarded, cell pellets were washed twice with PBS and incubated for 20min at RT with 4% formaldehyde. After two washes in PBS, samples were incubated with a blocking solution (PBS-BSA 3%) to prevent non-specific binding and then,1 hour a RT with the primary antibody EGFR (SC101, clone R1, Invitrogen) diluted 1:500 in PBS. Cells were washed three times with PBS and incubated 1 hour at RT with the secondary antibody Jackson Immunoresearch #115-025-062Rhodamine (TRITC)-AffiniPure Goat Anti-Mouse IgG (H+L) diluted 1:400 in PBS-BSA 2%. Samples were washed 3 times in PBS. The glass cover slide was then mounted on AttoFluor™ Cell Chamber (Thermo Fisher Scientific) and images were captured using confocal microscope Nikon A1R.

Phage-mediated targeting in ascitic samples

To evaluate phage targeting in patient-derived ascites, ascitic cells were seeded on glass coverslips and allowed to recover under standard culture conditions for 24 hours. Samples were then incubated with $M13_{7D12}$-CF594 (1 µM CF594 equivalents) for 45 minutes at 37 °C, washed twice with PBS to remove unbound phages, and maintained in phenol red-free medium for imaging. Nuclei were counterstained with Hoechst 33342 for 15 minutes prior to visualization. Live-cell confocal microscopy was performed

using a Nikon A1R system, monitoring CF594 fluorescence to assess phage binding and distribution within ascitic aggregates.

Cell viability determination in ascitic samples

Thawed ascitic fluid derived cells were resuspended in 10 mL of DMEM F12 culture medium and put in culture for 2 days to allow physiological recovery before cell viability analyses. After this time, tumor aggregates physiologically present in ascitic fluid were counted using a Neubauer chamber and seeded in round bottom ULA 96-well microplates (#7007 – Corning® Costar®) to obtain one tumor aggregate *per* well. 24 hours after seeding, samples were incubated with $M13_{7D12}$-RB (3 μM RB equivalents), free RB (3 μM), or PBS (control) for 45 minutes at 37 °C. Following incubation, samples were washed twice with PBS to remove unbound phages or sensitizer and subsequently irradiated for 3 minutes using a 565 nm LED source as described in the irradiation settings. After irradiation, samples were resuspended in complete medium and incubated for an additional 24 hours. Cell viability was then assessed using the CellTiter-Glo® 3D assay (Promega), according to the manufacturer's instructions.

To assess structural changes in ascitic aggregates following treatment, additional samples were processed for confocal imaging. Ascitic cells untreated or treated with $M13_{7D12}$-RB were stained with Hoechst 33342 for nuclear visualization and 24 hours post-treatment imaged using a Nikon A1R confocal microscope under identical acquisition settings. These analyses were used to evaluate treatment-induced alterations in the cytoarchitecture of ascitic aggregates, as reported in the Supplementary Information.

Statistical analysis

Unless otherwise specified, data are presented as mean ± SD from at least three independent experiments. Statistical analyses were performed using the tests indicated in each figure legend. GraphPad Prism version 10 (GraphPad Software, San Diego, CA, USA) was used for all analyses, and $p < 0.05$ was considered statistically significant.

Declarations

Ethics approval and consent to participate

All in vivo biodistribution experiments were performed in accordance with Italian and European regulations and approved by the Italian Ministry of Health (authorization 282/2024-PR). In vivo phage-mediated tumor photoablation experiments were reviewed and approved by the Experimental Animal Committee of the University of Helsinki and the Provincial Government of Southern Finland (license number ESAVI/6678/2019). Human ascitic fluid samples were obtained from a HGSOC patient collection enrolled in the MiPEO study (107_2011_U_Tess), approved by the local ethical committee at S. Orsola

Hospital, Bologna. Informed consent to participate was obtained from all patients enrolled in the study, in accordance with the approved protocol.

Consent for publication

Not applicable.

Competing interests

The authors declare no competing interests.

Funding

The research leading to these results has received funding from AIRC under MFAG 2019 - ID. 22894 project to M.C. The research is partly supported also by and by the European Union, NextGenerationEU, under project PRIN2022 Prot. 2022A5YWJJ to A.D, the Fondazione del Monte di Bologna e Ravenna (grant number 2023.0475; PhageLight project - P. I. Di Giosia Matteo) and by AIRC project IG2020 - ID. 24494 to A.M.P. M.S. is supported by the European Union - NextGenerationEU through the Italian Ministry of University and Research under PNRR - M4C2-I1.3Project PE_00000019“HEAL ITALIA.

Author Contribution

Conceptualization: P.E.C., M.N., M.D.G., M.C., V.C., A.D., P.L.L., A.M. Porcelli, A.M. Perrone, G.G. and C.F; Phage engineering, production and characterization: P.E.C., L.U., M.N., E.T., A.K., M.A., P.C. and A.P. Phage bioconjugation, ROS assays and mass spectrometry: R.S., A.C., A.M., P.E.C., C.D.D., M.D.S. and S.C. In vitro 2D and 3D experiments, imaging and flow cytometry: P.E.C., L.U., M.N., E.T., M.A., P.C. and A.P. In vivo mouse experiments: M.N., S.F., M.S.S., A.P. and L.U. Patient-derived ascites isolation, culture, characterization, imaging and ex vivo experiments: M.S., M.D.L., G.G., P.E.C. and A.M. Perrone. Data curation: P.E.C., L.U., M.N. and S.F. Writing – original draft: P.E.C., M.N. and A.D. Writing – review & editing: all authors. Supervision: M.D.G., M.C., V.C. and A.D. Funding acquisition: A.D., M.C., V.C., M.D.G., and A.M. Porcelli. All authors have read and approved the final version of the manuscript.

Data Availability

The data supporting the findings of this study are available from the corresponding authors upon reasonable request. Source data are provided with this paper.

References

1. Salmond GPC, Fineran PC. A century of the phage: past, present and future. Nat Rev Microbiol. 2015;13:777–86. https://doi.org/10.1038/NRMICRO3564.

2. Pirnay JP, Kutter E. Bacteriophages: it's a medicine, Jim, but not as we know it. Lancet Infect Dis. 2021;21:309–11. https://doi.org/10.1016/S1473-3099(20)30464-3.
3. Strathdee SA, Hatfull GF, Mutalik VK, Schooley RT. Phage therapy: From biological mechanisms to future directions. Cell. 2023;186:17–31. https://doi.org/10.1016/J.CELL.2022.11.017.
4. Pirnay JP, Djebara S, Steurs G, Griselain J, Cochez C, De Soir S, Glonti T, Spiessens A, Berghe V, Green E, S., et al. Personalized bacteriophage therapy outcomes for 100 consecutive cases: a multicentre, multinational, retrospective observational study. Nat Microbiol. 2024;9:1434–53. https://doi.org/10.1038/S41564-024-01705-X.
5. Dedrick RM, Guerrero-Bustamante CA, Garlena RA, Russell DA, Ford K, Harris K, Gilmour KC, Soothill J, Jacobs-Sera D, Schooley RT, et al. Engineered bacteriophages for treatment of a patient with a disseminated drug-resistant Mycobacterium abscessus. Nat Med. 2019;25:730–3. https://doi.org/10.1038/S41591-019-0437-Z.
6. Henry KA, Arbabi-Ghahroudi M, Scott JK. Beyond phage display: non-traditional applications of the filamentous bacteriophage as a vaccine carrier, therapeutic biologic, and bioconjugation scaffold. Front Microbiol. 2015;6:755. https://doi.org/10.3389/fmicb.2015.00755.
7. Foglizzo V, Marchiò S. Bacteriophages as Therapeutic and Diagnostic Vehicles in Cancer. Pharmaceuticals 2021. 2021;14:1–16. https://doi.org/10.3390/PH14020161.
8. Smith GP. Phage display: simple evolution in a petri dish (Nobel Lecture). Angew Chem Int Ed Engl. 2019;58:14428–37. https://doi.org/10.1002/ANIE.201908308.
9. Barderas R, Benito-Peña E. The 2018 Nobel Prize in Chemistry: phage display of peptides and antibodies. Anal Bioanal Chem. 2019;411:2475–9. https://doi.org/10.1007/s00216-019-01714-4.
10. Bortot B, Apollonio M, Baj G, Andolfi L, Zupin L, Crovella S, di Giosia M, Cantelli A, Saporetti R, Ulfo L, et al. Advanced photodynamic therapy with an engineered M13 phage targeting EGFR: Mitochondrial localization and autophagy induction in ovarian cancer cell lines. Free Radic Biol Med. 2022;179:242–51. https://doi.org/10.1016/J.FREERADBIOMED.2021.11.019.
11. Turrini E, Ulfo L, Costantini PE, Saporetti R, Di Giosia M, Nigro M, Petrosino A, Pappagallo L, Kaltenbrunner A, Cantelli A et al. (2024). Molecular engineering of a spheroid-penetrating phage nanovector for photodynamic treatment of colon cancer cells. Cell. Mol. Life Sci. *81*. https://doi.org/10.1007/s00018-024-05174-7
12. Ulfo L, Cantelli A, Petrosino A, Costantini PE, Nigro M, Starinieri F, Turrini E, Zadran SK, Zuccheri G, Saporetti R, et al. Orthogonal nanoarchitectonics of M13 phage for receptor targeted anticancer photodynamic therapy. Nanoscale. 2021;14:632–41. https://doi.org/10.1039/d1nr06053h.
13. Agostinis P, Berg K, Cengel KA, Foster TH, Girotti AW, Gollnick SO, Hahn SM, Hamblin MR, Juzeniene A, Kessel D, et al. Photodynamic therapy of cancer: An update. CA Cancer J Clin. 2011;61:250–81. https://doi.org/10.3322/CAAC.20114/FORMAT/PDF.
14. Lucky SS, Soo KC, Zhang Y. Nanoparticles in photodynamic therapy. Chem Rev. 2015;115:1990–2042. https://doi.org/10.1021/cr5004198.

15. Valko M, Izakovic M, Mazur M, Rhodes CJ, Telser J. Role of oxygen radicals in DNA damage and cancer incidence. Mol Cell Biochem. 2004;266:37–56. https://doi.org/10.1023/B:MCBI.0000049134.69131.89/METRICS.
16. Ulfo L, Costantini PE, Di Giosia M, Danielli A, Calvaresi M. EGFR-targeted photodynamic therapy. Pharmaceutics. 2022;14:241. https://doi.org/10.3390/PHARMACEUTICS14020241.
17. Costantini PE, Saporetti R, Iencharelli M, Flammini S, Montrone M, Sanità G, De Felice V, Mattioli EJ, Zangoli M, Ulfo L et al. (2025). Phage-Templated Synthesis of Targeted Photoactive 1D-Thiophene Nanoparticles. Small *21*, 2405832. https://doi.org/10.1002/smll.202405832
18. Zadran SK, Facchinello N, De Rosa P, Saporetti R, Costantini PE, Ulfo L, Nigro M, Petrosino A, Pappagallo L, Aloisi S et al. (2025). Systematic Targeting of GD2-Positive Neuroblastoma Tumors With a Photooncolytic Phage Nanovector Platform. Adv. Sci. (Weinh). *12*. https://doi.org/10.1002/ADVS.202415356
19. Uribe ML, Marrocco I, Yarden Y. (2021). EGFR in Cancer: Signaling Mechanisms, Drugs, and Acquired Resistance. Cancers 2021, Vol. 13, *13*. https://doi.org/10.3390/CANCERS13112748
20. Demartis S, Obinu A, Gavini E, Giunchedi P, Rassu G. Nanotechnology-based rose Bengal: a broad-spectrum biomedical tool. Dyes Pigm. 2021;188:109236. https://doi.org/10.1016/J.DYEPIG.2021.109236.
21. Wang B, Wang JH, Liu Q, Huang H, Chen M, Li K, Li C, Yu XF, Chu PK. Rose-bengal-conjugated gold nanorods for in vivo photodynamic and photothermal oral cancer therapies. Biomaterials. 2014;35:1954–66. https://doi.org/10.1016/J.BIOMATERIALS.2013.11.066.
22. Roovers RC, Vosjan MJWD, Laeremans T, El Khoulati R, De Bruin RCG, Ferguson KM, Verkleij AJ, Van Dongen GAMS, Van Bergen E, Henegouwen PMP. A biparatopic anti-EGFR nanobody efficiently inhibits solid tumour growth. Int J Cancer. 2011;129:2013–24. https://doi.org/10.1002/IJC.26145.
23. Rasmussen UB, Schreiber V, Schultz H, Mischler F, Schughart K. (2002). Tumor cell-targeting by phage-displayed peptides. Cancer Gene Therapy 2002 9:7 *9*, 606–612. https://doi.org/10.1038/sj.cgt.7700476
24. Kaltenbrunner A, Martino A, Nigro M, Carboni A, Marconi A, Mercorelli N, Di Sante M, Di Donato C, Petrosino A, Corrà S, et al. Conjugating M13 bacteriophage targeting folate receptor alpha with multiple photosensitizers: a flexible phototheranostic platform against ovarian cancer. J Mater Chem B. 2026. https://doi.org/10.1039/D5TB02844B.
25. Ding H, Yu H, Dong Y, Tian R, Huang G, Boothman DA, Sumer BD, Gao J. Photoactivation Switch from Type II to Type I Reactions by Electron-Rich Micelles for Improved Photodynamic Therapy of Cancer Cells Under Hypoxia. J Control Release. 2011;156:276. https://doi.org/10.1016/J.JCONREL.2011.08.019.
26. Dolmans DEJGJ, Fukumura D, Jain RK. Photodynamic therapy for cancer. Nat Rev Cancer. 2003;3:380–7. https://doi.org/10.1038/NRC1071.
27. Chen Z, Han F, Du Y, Shi H, Zhou W. Hypoxic microenvironment in cancer: molecular mechanisms and therapeutic interventions. Signal Transduct Target Ther. 2023;8:70.

https://doi.org/10.1038/S41392-023-01332-8.

28. Edmondson R, Broglie JJ, Adcock AF, Yang L. Three-dimensional cell culture systems and their applications in drug discovery and cell-based biosensors. Assay Drug Dev Technol. 2014;12:207–18. https://doi.org/10.1089/ADT.2014.573.
29. Nunes D, Ricardo S. Ovarian Cancer Ascites as a Liquid Tumor Microenvironment. Ovarian Cancer. 2022;43–55. https://doi.org/10. 36255/EXON-PUBLICATIONS-OVARIAN-CANCER-TUMOR-MICROENVIRONMENT.
30. Scott EM, Frost S, Khalique H, Freedman JD, Seymour LW, Lei-Rossmann J. (2020). Use of Liquid Patient Ascites Fluids as a Preclinical Model for Oncolytic Virus Activity. Methods Mol. Biol. *2058*, 261–270. https://doi.org/10.1007/978-1-4939-9794-7_17
31. Al Habyan S, Kalos C, Szymborski J, McCaffrey L. Multicellular detachment generates metastatic spheroids during intra-abdominal dissemination in epithelial ovarian cancer. Oncogene. 2018;37:5127–35. https://doi.org/10.1038/S41388-018-0317-X.
32. Capellero S, Erriquez J, Battistini C, Porporato R, Scotto G, Borella F, Di Renzo MF, Valabrega G, Olivero M. (2022). Ovarian Cancer Cells in Ascites Form Aggregates That Display a Hybrid Epithelial-Mesenchymal Phenotype and Allows Survival and Proliferation of Metastasizing Cells. Int. J. Mol. Sci. *23*. https://doi.org/10.3390/IJMS23020833
33. Kurelac I, Sollazzo M, De Luise M, Nanetti F, Lanteri L, D'Angelo L, Cavina B, Corrà S, Miglietta S, Milioni S et al. (2025). Immunomagnetic enrichment coupled to PAX8/TP53 molecular pathology approach increases sensitivity in the detection of ovarian cancer cells in ascites. Front. Mol. Biosci. *12*. https://doi.org/10.3389/FMOLB.2025.1537407
34. Hernández IB, Angelier ML, D'ondes TDB, Di Maggio A, Yu Y, Oliveira S. The potential of nanobody-targeted photodynamic therapy to trigger immune responses. Cancers (Basel). 2020;12:1–16. https://doi.org/10.3390/cancers12040978.
35. Mitchell MJ, Billingsley MM, Haley RM, Wechsler ME, Peppas NA, Langer R. Engineering precision nanoparticles for drug delivery. Nat Reviews Drug Discovery 2020. 2020;20(2 20):101–24. https://doi.org/10.1038/s41573-020-0090-8.
36. Calori IR, Bi H, Tedesco AC. Expanding the Limits of Photodynamic Therapy: The Design of Organelles and Hypoxia-Targeting Nanomaterials for Enhanced Photokilling of Cancer. ACS Appl Bio Mater. 2021;4:195–228. https://doi.org/10.1021/ACSABM.0C00945.
37. Sun M, Wang T, Li L, Li X, Zhai Y, Zhang J, Li W. The Application of Inorganic Nanoparticles in Molecular Targeted Cancer Therapy: EGFR Targeting. Front Pharmacol. 2021;12:702445. https://doi.org/10.3389/fphar.2021.702445.
38. Nguyen PV, Hervé-Aubert K, Chourpa I, Allard-Vannier E. Active targeting strategy in nanomedicines using anti-EGFR ligands - A promising approach for cancer therapy and diagnosis. Int J Pharm. 2021;609:121134. https://doi.org/10.1016/j.ijpharm.2021.121134.
39. Roskoski R. The ErbB/HER family of protein-tyrosine kinases and cancer. Pharmacol Res. 2014;79:34–74. https://doi.org/10.1016/J.PHRS.2013.11.002.

40. Nicholson RI, Gee JMW, Harper ME. (2001). EGFR and cancer prognosis. Eur. J. Cancer *37 Suppl 4*, 9. https://doi.org/10.1016/S0959-8049(01)00231-3

41. Peng W, de Bruijn HS, ten Hagen TLM, van Dam GM, Roodenburg JLN, Berg K, Witjes MJH, Robinson DJ. Targeted Photodynamic Therapy of Human Head and Neck Squamous Cell Carcinoma with Anti-epidermal Growth Factor Receptor Antibody Cetuximab and Photosensitizer IR700DX in the Mouse Skin-fold Window Chamber Model. Photochem Photobiol. 2020;96:708–17. https://doi.org/10.1111/php.13267.

42. Huang S, He Y, Madow A, Peng H, Griffin M, Qi J, Huang M, Amoroso H, Abrashoff R, Heldman N, et al. A Programmable Nanovaccine Platform Based on M13 Bacteriophage for Personalized Cancer Vaccine and Therapy. Adv Mater. 2025;37:e10229. https://doi.org/10.1002/ADMA.202510229.

43. Petrenko VA, Gillespie JW, Petrenko V, Gillespie JW. Paradigm shift in bacteriophage-mediated delivery of anticancer drugs: from targeted magic bullets to self-navigated magic missiles. Expert Opin. Drug Deliv. 2016;14:373. https://doi.org/10.1080/17425247.2016.1218463.

44. Van Driel PBAA, Boonstra MC, Slooter MD, Heukers R, Stammes MA, Snoeks TJA, De Bruijn HS, Van Diest PJ, Vahrmeijer AL, Van Bergen PMP et al. (2016). EGFR targeted nanobody-photosensitizer conjugates for photodynamic therapy in a pre-clinical model of head and neck cancer. Journal of Controlled Release *229*, 93–105. https://doi.org/10.1016/j.jconrel.2016.03.014

45. van Lith SAM, van den Brand D, Wallbrecher R, Wübbeke L, van Duijnhoven SMJ, Mäkinen PI, Hoogstad-van Evert JS, Massuger L, Ylä-Herttuala S, Brock R, et al. The effect of subcellular localization on the efficiency of EGFR-targeted VHH photosensitizer conjugates. Eur J Pharm Biopharm. 2018;124:63–72. https://doi.org/10.1016/j.ejpb.2017.12.009.

46. Mashayekhi V, Xenaki KT, van Bergen PMP, Oliveira S. Dual targeting of endothelial and cancer cells potentiates in vitro nanobody-targeted photodynamic therapy. Cancers (Basel). 2020;12:1–18. https://doi.org/10.3390/cancers12102732.

47. Xiong T, Peng Q, Chen Y, Li M, Du J, Fan J, Jia L, Peng X. A Novel Nanobody–Photosensitizer Conjugate for Hypoxia Resistant Photoimmunotherapy. Adv Funct Mater. 2021;31:1–10. https://doi.org/10.1002/adfm.202103629.

48. Schmitz KR, Bagchi A, Roovers RC, Van Bergen En Henegouwen PMP, Ferguson KM. (2013). Structural evaluation of EGFR inhibition mechanisms for nanobodies/VHH domains. Structure *21*, 1214–1224. https://doi.org/10.1016/j.str.2013.05.008

49. Goh LK, Sorkin A. (2013). Endocytosis of Receptor Tyrosine Kinases. Cold Spring Harb. Perspect. Biol. *5*, a017459. https://doi.org/10.1101/CSHPERSPECT.A017459

50. Nguyen S, Baker K, Padman BS, Patwa R, Dunstan RA, Weston TA, Schlosser K, Bailey B, Lithgow T, Lazarou M et al. (2017). Bacteriophage Transcytosis Provides a Mechanism To Cross Epithelial Cell Layers. mBio *8*. https://doi.org/10.1128/MBIO.01874-17

51. Hajitou A, Trepel M, Lilley CE, Soghomonyan S, Alauddin MM, Marini FC, Restel BH, Ozawa MG, Moya CA, Rangel R et al. (2006). A Hybrid Vector for Ligand-Directed Tumor Targeting and Molecular Imaging. Cell *125*, 385–398. https://doi.org/10.1016/j.cell.2006.02.042

52. Bichet MC, Chin WH, Richards W, Lin YW, Avellaneda-Franco L, Hernandez CA, Oddo A, Chernyavskiy O, Hilsenstein V, Neild A et al. (2021). Bacteriophage uptake by mammalian cell layers represents a potential sink that may impact phage therapy. iScience *24*. https://doi.org/10.1016/J.ISCI.2021.102287
53. Douadi C, Lamy-Besnier Q, Theodorou I, Schiettekatte O, Sbardella Y, Brot L, Costantini PE, Saporetti R, Danielli A, Calvaresi M, et al. Differential translocation of bacteriophages across the intestinal barrier in health and Crohn's disease. Cell Rep 45. 2026. https://doi.org/10.1016/j.celrep.2025.116726.
54. Shen Y, Wang J, Li Y, Yang CT, Zhou X. (2023). Modified Bacteriophage for Tumor Detection and Targeted Therapy. Nanomaterials (Basel) *13*. https://doi.org/10.3390/NANO13040665
55. Nessler I, Menezes B, Thurber GM. Key metrics to expanding the pipeline of successful antibody–drug conjugates. Trends Pharmacol Sci. 2021;42:803–12. https://doi.org/10.1016/j.tips.2021.07.005.
56. El-Tanani M, Rabbani SA, Babiker R, Rangraze I, Kapre S, Palakurthi SS, Alnuqaydan AM, Aljabali AA, Rizzo M, El-Tanani Y, et al. Unraveling the tumor microenvironment: Insights into cancer metastasis and therapeutic strategies. Cancer Lett. 2024;591:216894. https://doi.org/10.1016/J.CANLET.2024.216894.
57. Tsedev U, Lin CW, Hess GT, Sarkaria JN, Lam FC, Belcher AM. Phage Particles of Controlled Length and Genome for In Vivo Targeted Glioblastoma Imaging and Therapeutic Delivery. ACS Nano. 2022;16:11676–91. https://doi.org/10.1021/ACSNANO.1C08720.
58. Skorzynski M, Krol M, Braniewska A. Hepatotoxicity of Nanoparticle-Based Anti-Cancer Drugs: Insights into Toxicity and Mitigation Strategies. Int J Nanomed. 2025;20:11697–715. https://doi.org/10.2147/IJN.S543433.
59. Kondrashov A, Sapkota S, Sharma A, Riano I, Kurzrock R, Adashek JJ. (2023). Antibody-Drug Conjugates in Solid Tumor Oncology: An Effectiveness Payday with a Targeted Payload. Pharmaceutics *15*. https://doi.org/10.3390/PHARMACEUTICS15082160
60. Bayram D, Uçar G. (2024). Hepatotoxicity of Anti-cancer Drugs. 549–78. https://doi.org/10.1007/16833_2024_344
61. Baroyan NV. Method for evaluating the total absorption-excretion function of thew liver clearance curves for the indicators indocyanine green and 131I-rose bengal in blood. Exp Med. 1985;20:74–8.
62. Cheng Q, Tucker EI, Pine MS, Sisler I, Matafonov A, Sun MF, White-Adams TC, Smith SA, Hanson SR, McCarty OJT, et al. A role for factor XIIa-mediated factor XI activation in thrombus formation in vivo. Blood. 2010;116:3981–9. https://doi.org/10.1182/BLOOD-2010-02-270918.
63. He L, Vicente CP, Westrick RJ, Eitzman DT, Tollefsen DM. Heparin cofactor II inhibits arterial thrombosis after endothelial injury. J Clin Invest. 2002;109:213. https://doi.org/10.1172/JCI13432.
64. Klaassen CD. Pharmacokinetics of rose bengal in the rat, rabbit, dog, and guinea pig. Toxicol Appl Pharmacol. 1976;38:85–100. https://doi.org/10.1016/0041-008X(76)90163-0.

65. Ahmed H, Lopez H, Boselli F, Tarricone G, Vercellino S, Costantini PE, Castagnola V, Veronesi M, Benfenati F, Danielli A, et al. Biomimetic Plasmonic Nanophages by Head/Tail Self-Assembling: Gold Nanoparticle/Virus Interactions. ACS Nano. 2024;18:21302–15. https://doi.org/10.1021/ACSNANO.4C05198.
66. Feng F, Han X, Fang Z, Xi K, Wang Z, Shen J, Zhang Y, Wang M, Li Z, Han X et al. (2026). Synthetic M13 phage engagers expand CAR-T cell antigen recognition to overcome tumor heterogeneity. Trends Biotechnol. *0*. https://doi.org/10.1016/j.tibtech.2026.02.008
67. Krysko DV, Garg AD, Kaczmarek A, Krysko O, Agostinis P, Vandenabeele P. Immunogenic cell death and DAMPs in cancer therapy. Nat Rev Cancer. 2012;2012 12(12 12):860–75. https://doi.org/10.1038/nrc3380.
68. Mishchenko T, Balalaeva I, Gorokhova A, Vedunova M, Krysko DV. Which cell death modality wins the contest for photodynamic therapy of cancer? Cell Death Dis. 2022;13:455. https://doi.org/10.1038/S41419-022-04851-4.
69. Kobayashi H, Choyke PL. Near-Infrared Photoimmunotherapy of Cancer. Acc Chem Res. 2019;52:2332–9. https://doi.org/10.1021/acs.accounts.9b00273.
70. Mitsunaga M, Ogawa M, Kosaka N, Rosenblum LT, Choyke PL, Kobayashi H. Cancer cell-selective in vivo near infrared photoimmunotherapy targeting specific membrane molecules. Nat Med. 2011;17:1685–91. https://doi.org/10.1038/nm.2554.
71. Kim MM, Darafsheh A. Light Sources and Dosimetry Techniques for Photodynamic Therapy. Photochem Photobiol. 2020;96:280–94. https://doi.org/10.1111/PHP.13219.
72. Evans CL. Three-dimensional in vitro cancer spheroid models for photodynamic therapy: Strengths and opportunities. Front Phys. 2015;3:135044. https://doi.org/10.3389/FPHY.2015.00015/TEXT.
73. Cantelli A, Malferrari M, Solda A, Simonetti G, Forni S, Toscanella E, Mattioli EJ, Zerbetto F, Zanelli A, Di Giosia M, et al. Human serum albumin-oligothiophene bioconjugate: a phototheranostic platform for localized killing of cancer cells by precise light activation. JACS Au. 2021;1:925–35. https://doi.org/10.1021/JACSAU.1C00061.
74. Mohammad-Hadi L, MacRobert AJ, Loizidou M, Yaghini E. Photodynamic therapy in 3D cancer models and the utilisation of nanodelivery systems. Nanoscale. 2018;10:1570–81. https://doi.org/10.1039/C7NR07739D.
75. Castano AP, Mroz P, Hamblin MR. Photodynamic therapy and anti-tumour immunity. Nat Rev Cancer. 2006;6:535–45. https://doi.org/10.1038/NRC1894.
76. Li M, Xu Y, Peng X, Kim JS. From Low to No O2-Dependent Hypoxia Photodynamic Therapy (hPDT): A New Perspective. Acc Chem Res. 2022;55:3253–64. https://doi.org/10.1021/ACS.ACCOUNTS.2C00531.
77. Brown JM, Wilson WR. Exploiting tumour hypoxia in cancer treatment. Nat Rev Cancer. 2004;4:437–47. https://doi.org/10.1038/NRC1367.
78. Rickard BP, Conrad C, Sorrin AJ, Ruhi MK, Reader JC, Huang SA, Franco W, Scarcelli G, Polacheck WJ, Roque DM et al. (2021). Malignant Ascites in Ovarian Cancer: Cellular, Acellular, and Biophysical

Determinants of Molecular Characteristics and Therapy Response. Cancers (Basel). *13*. https://doi.org/10.3390/CANCERS13174318

79. Shield K, Ackland ML, Ahmed N, Rice GE. Multicellular spheroids in ovarian cancer metastases: Biology and pathology. Gynecol Oncol. 2009;113:143–8. https://doi.org/10.1016/j.ygyno.2008.11.032.
80. Torres-Acosta M, González-Mora A, Ruiz-Ruiz F, Rito-Palomares M, Benavides J. Economic evaluation of M13 bacteriophage production at large-Scale for therapeutic applications using aqueous Two-Phase systems. J Chem Technol Biotechnol. 2020;95:2822–33. https://doi.org/10.1002/JCTB.6526. ;JOURNAL:JOURNAL:10974660;WGROUP:STRING:PUBLICATION.
81. Rakonjac J, Bennett NJ, Spagnuolo J, Gagic D, Russel M. (2011). Filamentous Bacteriophage: Biology, Phage Display and Nanotechnology Applications. Current Issues in Molecular Biology 2011, Vol. 13, Pages 51–76 *13*, 51–76. https://doi.org/10.21775/CIMB.013.051
82. Roux S, Hallam SJ, Woyke T, Sullivan MB. (2015). Viral dark matter and virus-host interactions resolved from publicly available microbial genomes. Elife *4*. https://doi.org/10.7554/ELIFE.08490
83. Petrosino A, Saporetti R, Starinieri F, Sarti E, Ulfo L, Boselli L, Cantelli A, Morini A, Zadran SK, Zuccheri G et al. (2023). A modular phage vector platform for targeted photodynamic therapy of Gram-negative bacterial pathogens. iScience *26*. https://doi.org/10.1016/j.isci.2023.108032
84. Smith GP, Scott JK. Libraries of Peptides and Proteins Displayed on Filamentous Phage. Methods Enzymol. 1993;217:228–57. https://doi.org/10.1016/0076-6879(93)17065-D.
85. Wessel D, Flügge UI. A method for the quantitative recovery of protein in dilute solution in the presence of detergents and lipids. Anal Biochem. 1984;138:141–3. https://doi.org/10.1016/0003-2697(84)90782-6.
86. Doucette AA, Vieira DB, Orton DJ, Wall MJ. Resolubilization of Precipitated Intact Membrane Proteins with Cold Formic Acid for Analysis by Mass Spectrometry. J Proteome Res. 2014;13:6001–12. https://doi.org/10.1021/PR500864A.
87. Marty MT, Baldwin AJ, Marklund EG, Hochberg GKA, Benesch JLP, Robinson CV. Bayesian deconvolution of mass and ion mobility spectra: from binary interactions to polydisperse ensembles. Anal Chem. 2015;87:4370–6. https://doi.org/10.1021/ACS.ANALCHEM.5B00140.

Figures

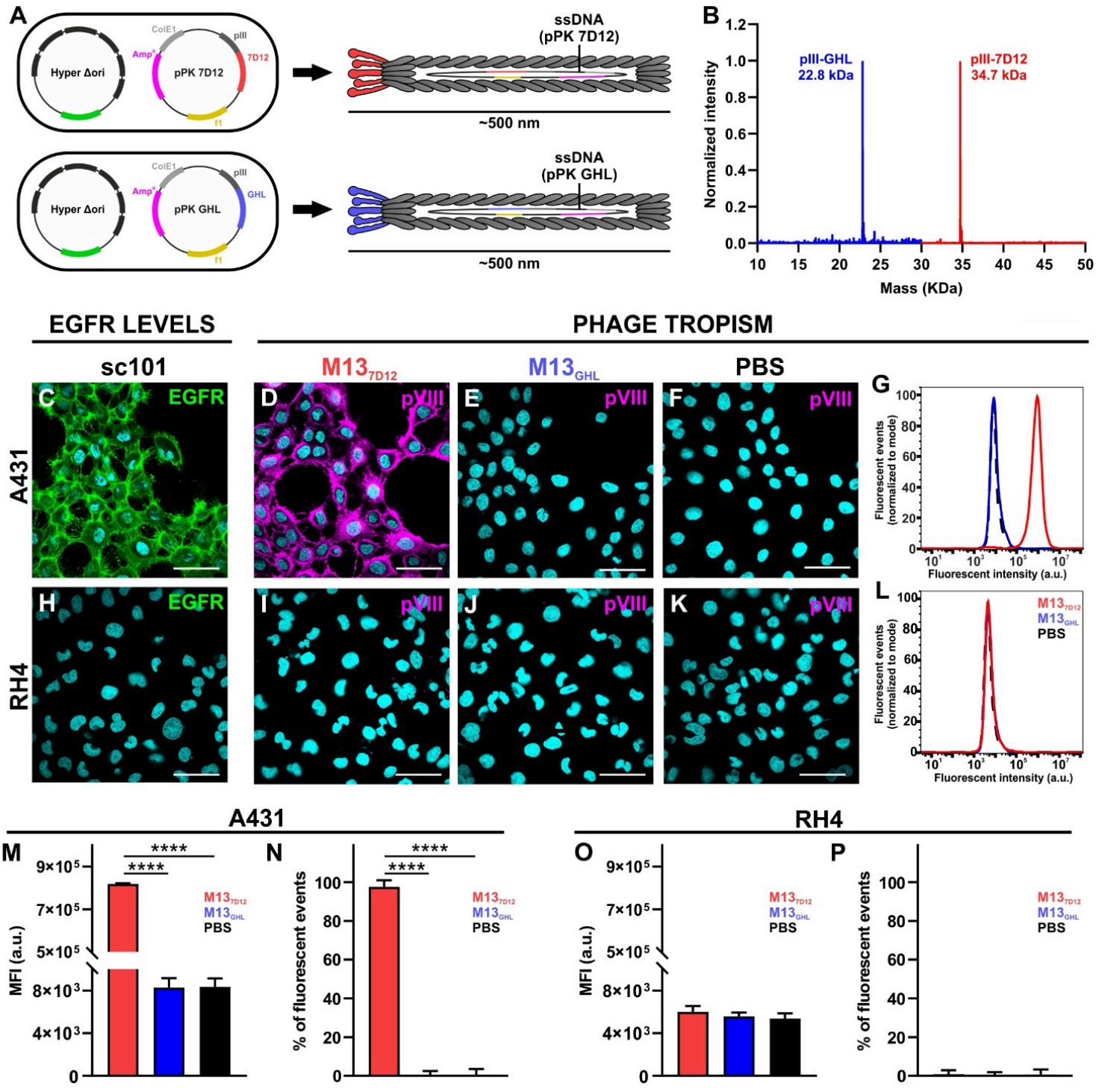


Figure 1

Generation and specific EGFR targeting of M13$_{7D12}$ phage nanobot. A, Scheme of phage genetic engineering through co-transformation in *E. coli* of both phagemid (either pPK_7D12 or pPK_GHL) and hyperphage genome. **B**, deconvoluted mass spectra of the pIII coat protein in M13$_{GHL}$ (blue) and M13$_{7D12}$ (red). EGFR expression of A431 (**C**) and RH4 (**H**) in confocal microscopy. EGFR in green and nuclei in cyan. Immunohistochemical confocal microscopy of A431 (**D**, **E**, **F**) and RH4 (**I**, **J**, **K**) cell lines incubated with M13$_{7D12}$ (**D**, **I**), M13$_{GHL}$ (**E**, **J**), and PBS (**F**, **K**). The major coat protein pVIII of M13 is in magenta while nuclei are in cyan. Scale bar = 50 µm. Quantitative analysis was performed in

immunohistochemistry on A431 (**G**, **M**) and RH4 (**L**, **O**) incubated with $M13_{7D12}$ (red), $M13_{GHL}$ (blue) and, PBS (black). Results are expressed as shift of the fluorescence peak (**G**, **L**), Mean fluorescence intensity (**M**, **O**) and percentage of fluorescent event (**N**, **P**). Statistical significance was assessed by one-way ANOVA with Tukey's multiple comparison test; ****p < 0.0001

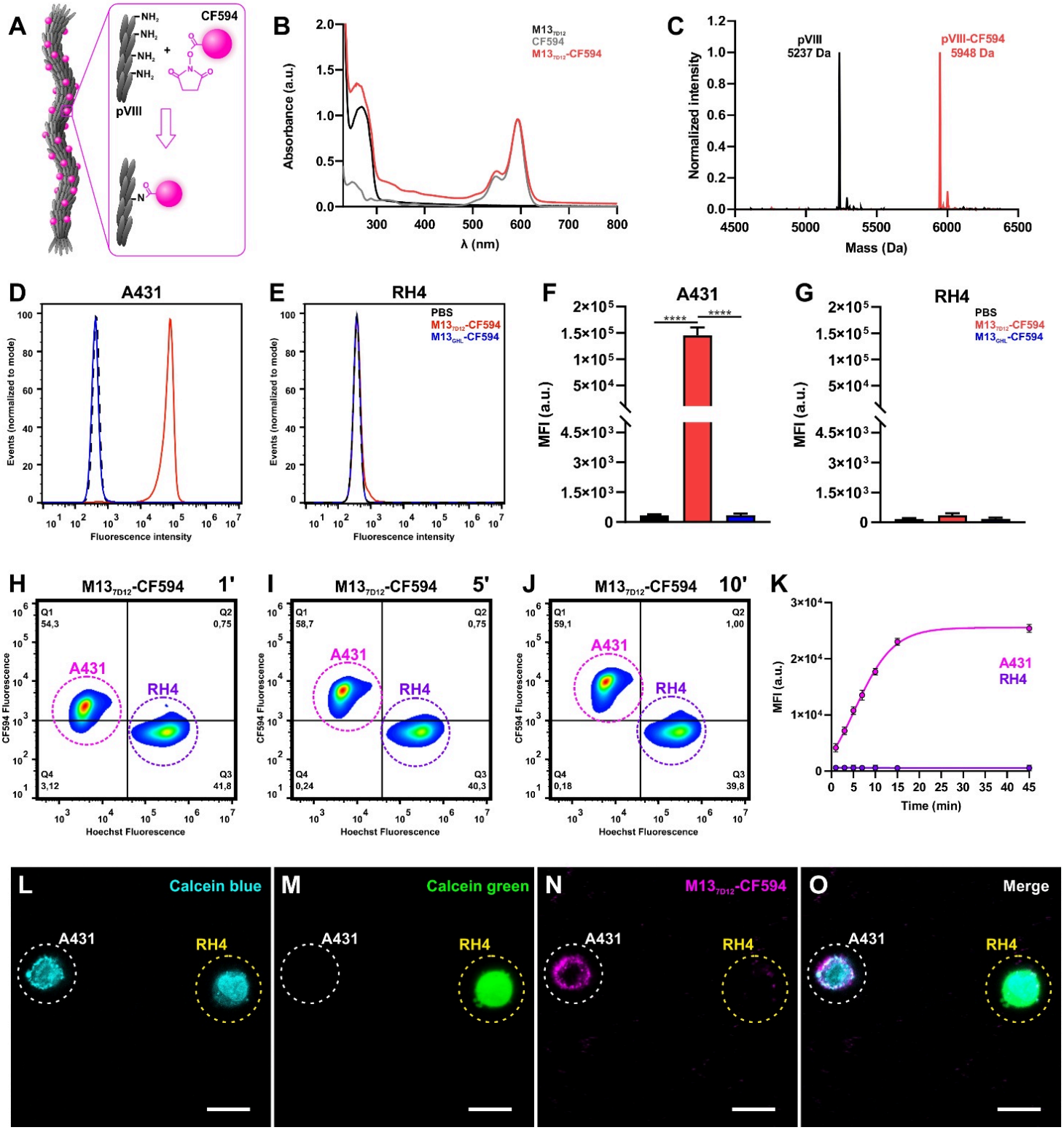


Figure 2

Specific payload delivery by $M13_{7D12}$. A, Scheme of the chemical engineering of M13 with CF594. **B,** UV-Vis spectrum of $M13_{7D12}$ (black), CF594 (grey) and bioconjugated $M13_{7D12}$-CF594. **C**, deconvoluted mass spectra of the $M13_{7D12}$-CF594 displaying the native PVIII (black) and conjugated pVIII-CF594 (red) coat proteins. $M13_{7D12}$-CF594 in red, unconjugated phages are in dark grey and free CF594 is in light grey. Flow cytometry was performed on A431 (**D**, **F**) and RH4 (**E**, **G**) preincubated with $M13_{7D12}$-CF594 (red), $M13_{GHL}$-CF594 (blue), and PBS (black). Results are shown as fluorescence shift peak (**D**, **E**) and mean fluorescence intensity (**F**, **G**). Statistical significance was assessed by one-way ANOVA with Tukey's multiple comparison test. **** $p < 0.0001$. Competitive experiments on mixed cultures of A431 (highlighted in magenta) and RH4 (highlighted in purple), this latter pre-incubated with Hoechst, in the presence of $M13_{7D12}$-CF594. Samples were analysed 1 min (**H**), 5 min (**I**) or 10 min (**J**) after the addition of the conjugated phage. Fluorescence in the Hoechst channel is shown on the x-axis, while the CF594 fluorescence channel is shown on the y-axis. **K**, Kinetics of the mean fluorescence intensity detected in the mixed culture of A431 (magenta) and RH4 (purple) incubated with $M13_{7D12}$-CF594. **L**-**O**, Confocal microscopy of A431 (highlighted in white) and RH4 (highlighted in yellow) mixed cultures after the addition of $M13_{7D12}$-CF594. **L**, calcein blue channel; **M**, calcein green channel, **N**, CF594 channel and, **O**, merge. Scale bar= 50 µm.

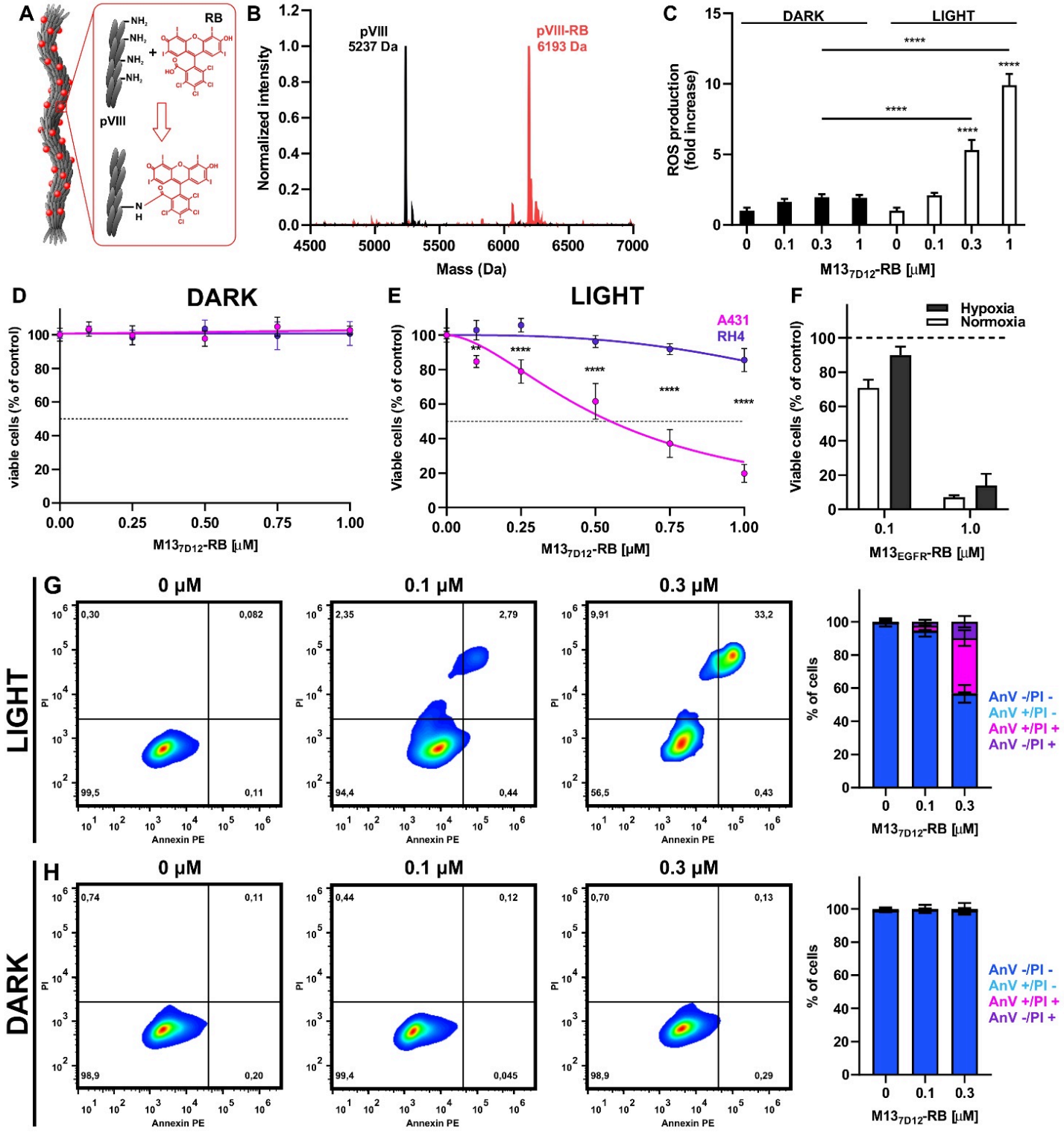


Figure 3

Targeted light-triggered cytotoxicity mediated by M13$_{7D12}$ in 2D cell cultures. A, Schematic representation of the chemical bioengineering conjugation of RB to the M13$_{7D12}$ with pVIII coat protein. **B**, Deconvoluted mass spectra of the M13$_{7D12}$ pVIII coat protein before and after conjugation with RB. **C**, Quantification of the intracellular ROS generated in the A431 cell line, using the ROS-Glo assay

(Promega). The cells preincubated with $M13_{7D12}$-RB were irradiated (white columns) for 1 minute with a single wavelength LED or kept in the dark, under the same conditions (black columns). **** $p < 0.0001$. Cytotoxic effects of $M13_{7D12}$-RB on A431 (magenta) and RH4 (purple) cells kept in the dark (**D**) or irradiated for 1 min with 565 nm LED source (**E**). The cytotoxic effect of the treatment was also evaluated in hypoxia and compared to the same treatment in normoxia (**F**). **** $p < 0.0001$. Cell death mechanisms induced by $M13_{7D12}$-RB at 0 µM, 0.1 µM and 0.3 µM (RB equivalents) were analysed in samples either (**G**) irradiated or (**H**) kept in dark. Flow cytometry dot plots show Annexin V (AnV) fluorescence on the x-axis and propidium iodide (PI) fluorescence on the y-axis. Histograms represent the percentage of AnV−/PI- (blue), AnV+/PI- (cyan), AnV+/PI+ (magenta), AnV−/PI+ (purple). For ROS quantification (C), statistical significance was assessed by two-way ANOVA followed by Dunnett's multiple comparison test versus the corresponding non-irradiated control. For cell viability assays (D, E), statistical significance was assessed by two-way ANOVA followed by Šídák's multiple comparison test between A431 and RH4 cells at each concentration, while for hypoxia experiments (F), statistical significance was assessed by unpaired two-tailed t-test.

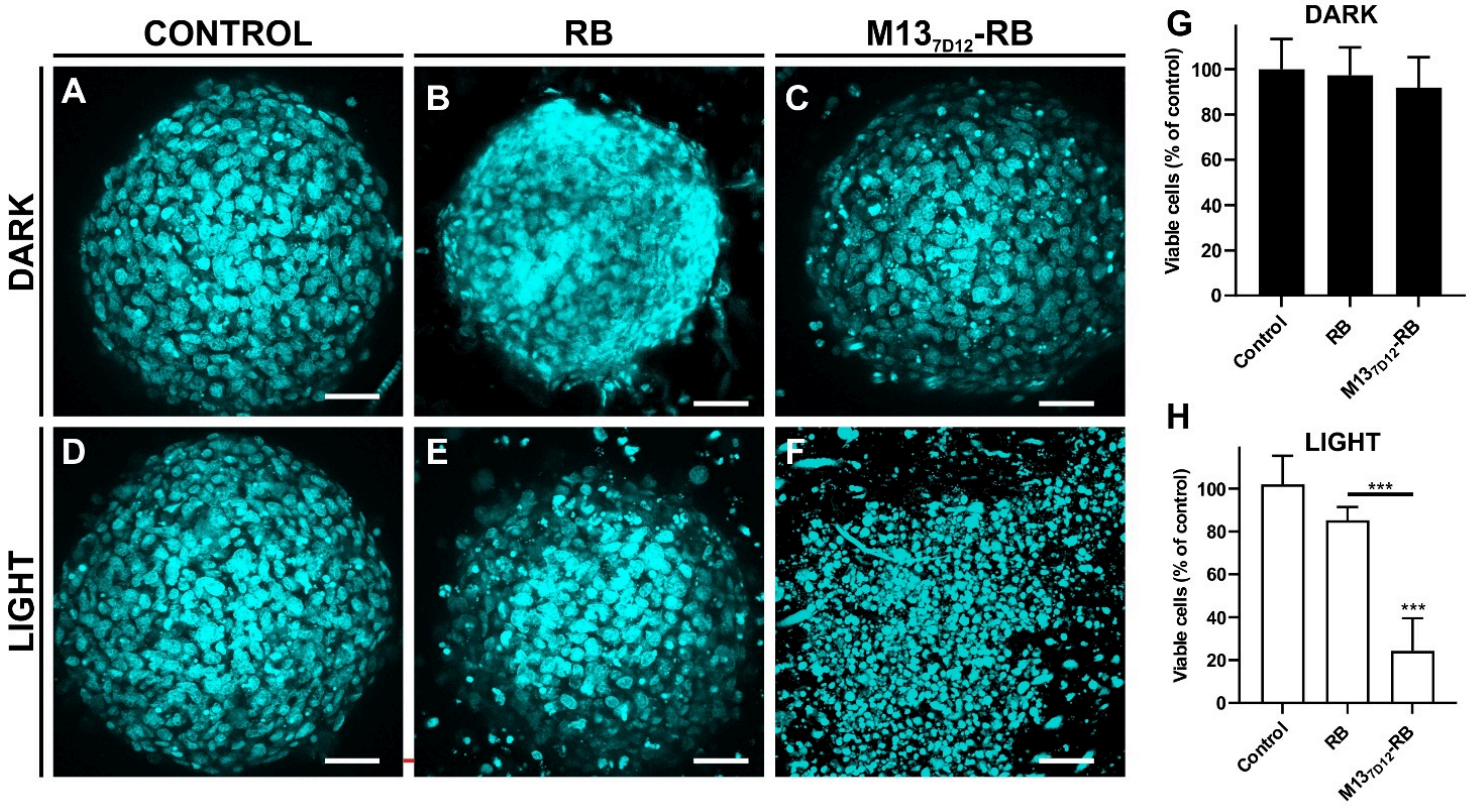


Figure 4

Phage-mediated targeted photo-oncolytic disruption of tumor spheroids. Evaluation of the cytoarchitecture of A431 spheroid incubated with PBS (control, **A**, **D**), free-RB (**B**, **E**) or $M13_{7D12}$-RB (**C**, **F**). Spheroids were kept in dark conditions (**A**-**C**) or irradiated with the 565 nm LED source for 3 min (**D**-**F**). Hoechst in cyan. Scale bar= 50 µm. Cell viability was evaluated with 3D CellTiter-Glo® on spheroids pre-incubated with PBS, free-RB or $M13_{7D12}$-RB and kept in dark (**G**) or irradiated (**H**). Statistical significance

was assessed by one-way ANOVA followed by Tukey's multiple comparison test. Asterisks above bars indicate significance versus the control, *** $p < 0.001$.

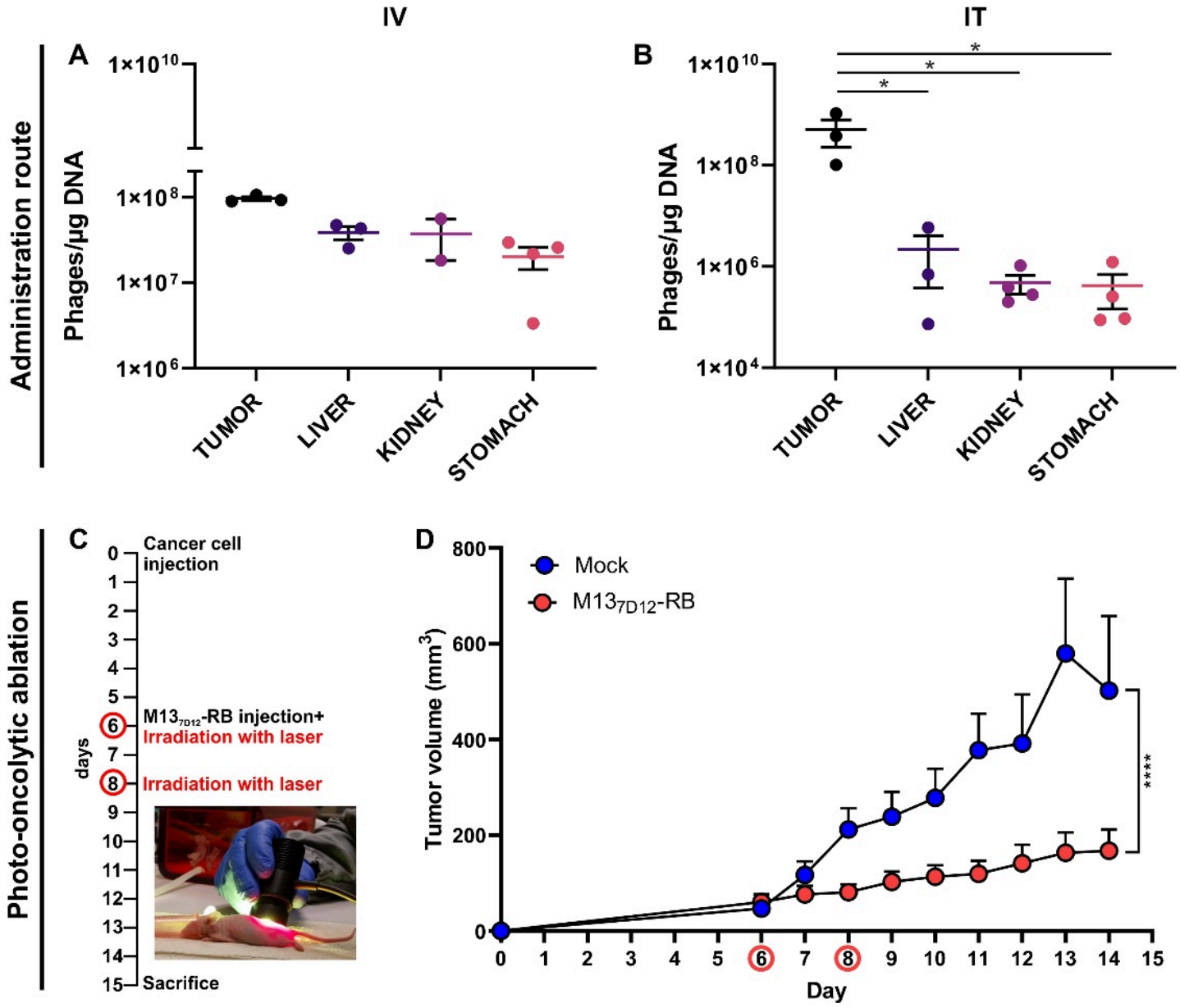


Figure 5

Phage administration route and tumor burden reduction upon light activation *in vivo*. Biodistribution of $M13_{7D12}$ phage nanobots in nude mice following (**A**) intravenous (IV) or (**B**) intratumoral (IT) administration. Phage accumulation was quantified 24 hours post-injection by quantitative real-time PCR in tumor, liver, kidney and stomach tissues. Statistical significance was assessed by one-way ANOVA followed by Dunnett's multiple comparison test versus tumor; * $p < 0.05$. **C**, Schematic representation of the *in vivo* experiment design and timeline. $M13_{7D12}$-RB was administered once by intratumoral injection at day 6, followed by light irradiation at day 6 and day 8. **D**, Tumor volume progression in mice receiving intratumoral $M13_{7D12}$-RB followed by light irradiation (red) or mock-treated mice injected with PBS and

not irradiated (blue). Results are expressed as mean ± SEM. Statistical significance was assessed by two-way repeated-measures ANOVA followed by Šídák's multiple comparison test between groups; **** $p < 0.0001$.

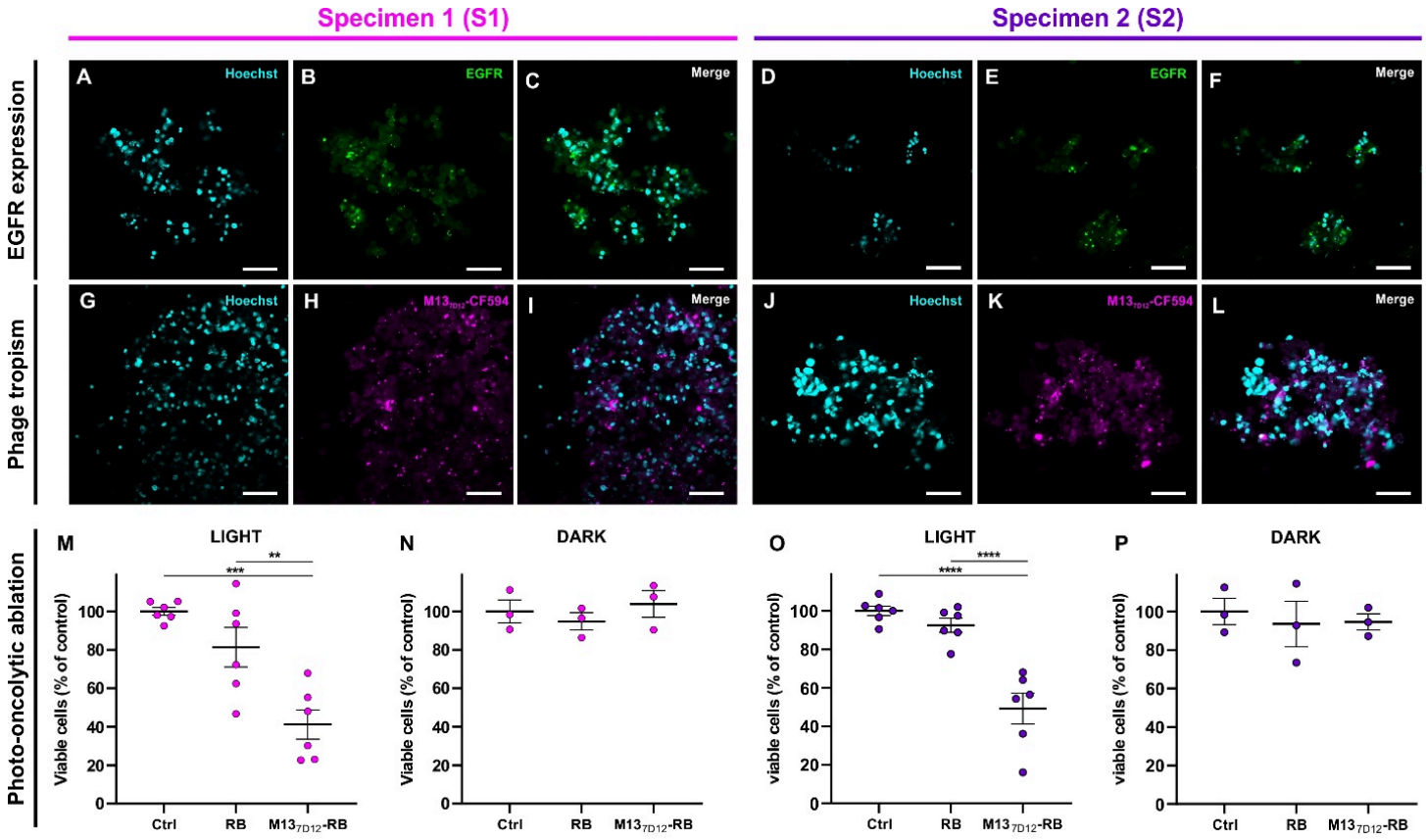


Figure 6

EGFR expression, phage targeting and phage-mediated photoablation in HGSOC-derived ascitic fluid. **A**-**F**, EGFR expression in malignant ascites derived from two HGSOC patients was evaluated by immunocytochemistry. **A**, **D**, nuclei tagged with Hoechst 33342 in cyan; **B**, **E**, EGFR in green; **C**, **F**, merge images. **G**-**L**. Targeting of conjugated $M13_{7D12}$ on malignant ascites. **G**, **J**, nuclei in cyan; **H**, **K**, CF594 in magenta; **I**, **L**, merge images. Scale bar = 50 µm. **M**-**P**, Cell viability of HGSOC-derived ascites pre-incubated with PBS (Ctrl), free RB, or $M13_{7D12}$-RB, and either irradiated (**M**, **O**) or kept in the dark (**N**, **P**), as assessed by CellTiter-Glo® 3D assay. Statistical significance was assessed by one-way ANOVA followed by Tukey's multiple comparison test; **p<0.01, ***p< 0.001, **** p < 0.0001.

Supplementary Files

This is a list of supplementary files associated with this preprint. Click to download.

- SILighttriggerablenanobots.docx